

1 **Can mesoscale eddy kinetic energy sources and sinks be
2 inferred from sea surface height in the Agulhas Current
3 region?**

4 **P. Tedesco^{1,2}, J. Gula^{1,3}, P. Penven¹, C. Ménesguen¹, Q. Jamet⁴, C. Vic¹**

5 ¹Univ. Brest, CNRS, IRD, Ifremer, Laboratoire d'Océanographie Physique et Spatiale (LOPS), IUEM,
6 29280, Brest, France.

7 ²University of Cambridge, Cambridge, UK.

8 ³Institut Universitaire de France (IUF), Paris, France.

9 ⁴INRIA, ODYSSEY group, Ifremer, Plouzané, France.

10 **Key Points:**

- 11 • We assess whether the mesoscale eddy energy flux divergence can be calculated from
12 sea surface height in the Agulhas Current region
- 13 • Geostrophy allows a qualitative estimate of eddy energy advection, but not of eddy
14 pressure work
- 15 • This favours the use of sea surface height, but challenges the founding approximations
16 of an earlier paradigm
- 17
- 18
- 19

Corresponding author: Pauline Tedesco, pfmt2@cam.ac.uk

20 **Abstract**

21 Western boundaries have been suggested as mesoscale eddy graveyards, using a diagnostic
 22 of the eddy kinetic energy (*EKE*) flux divergence based on sea surface height (η). The
 23 graveyard's paradigm relies on the approximation of geostrophy — required by the use of
 24 η — and other approximations that support long baroclinic Rossby waves as the dominant
 25 contribution to the *EKE* flux divergence. However, a recent study showed an opposite
 26 paradigm in the Agulhas Current region using an unapproximated *EKE* flux divergence.
 27 Here, we assess the validity of the approximations used to derive the η -based *EKE* flux
 28 divergence using a regional numerical simulation of the Agulhas Current. The *EKE* flux
 29 divergence consists of the eddy pressure work (*EPW*) and the *EKE* advection (*AEKE*).
 30 We show that geostrophy is valid for inferring *AEKE*, but that all approximations are
 31 invalid for inferring *EPW*. A scale analysis shows that at mesoscale ($L > O(30)$ km), *EPW*
 32 is dominated by coupled geostrophic-ageostrophic *EKE* flux and that Rossby waves effect
 33 is weak. There is also a hitherto neglected topographic contribution, which can be locally
 34 dominant. *AEKE* is dominated by the geostrophic *EKE* flux, which makes a substantial
 35 contribution (54%) to the net regional mesoscale *EKE* source represented by the *EKE* flux
 36 divergence. Other contributions, including topographic and ageostrophic effects, are also
 37 significant. Our results support the use of η to infer a qualitative estimate of the *EKE* flux
 38 divergence in the Agulhas Current region. However, they invalidate the approximations on
 39 mesoscale eddy dynamics that underlie the graveyard's paradigm.

40 **Plain Language Summary**

41 In the ocean, the most energetic motions are large-scale eddies with horizontal scales
 42 ranging from tens to hundreds of kilometers. These are major components of the ocean
 43 energy budget, and unravelling their lifecycles is crucial to improving our understanding
 44 of ocean dynamics. Although the generation of large-scale eddies is well documented, how
 45 their energy is dissipated remains uncertain. Based on satellite observations of the sea
 46 surface and approximations to the dynamics of large-scale eddies, it has been suggested
 47 that they decay at western boundaries of oceanic basins, thereby closing their lifecycle.
 48 However, based on different data and approximations, a recent study has suggested that
 49 large-scale eddies are predominantly generated in a specific western boundary region, such
 50 as the Agulhas Current. Our study explains which of the data (sea surface observations)
 51 or the assumed leading order dynamics (approximations) explains the opposite eddy energy
 52 sources and sinks shown by the two studies in the Agulhas Current region. Our results show
 53 that the use of sea surface observations is valid for qualitatively inferring the regional eddy
 54 energy source, but not the assumed leading order dynamics. This has implications for (1)
 55 our understanding and (2) study strategies of the energetics of large-scale eddies.

56 1 Introduction

57 Mesoscale eddies account for 80 % of the surface kinetic energy and are a key component
 58 of the global ocean energy budget (Wunsch, 2007; Ferrari & Wunsch, 2009; Müller et al.,
 59 2005). They have horizontal scales of the order of the 1st Rossby deformation radius (Rd)
 60 or larger (Chelton et al., 2011). At these scales, the velocity field can be decomposed
 61 into a leading order geostrophic and a weaker ageostrophic component, following the quasi-
 62 geostrophic theory (Gill, 1982). Geostrophic flows are horizontally divergence-free flows
 63 — in a local approximation — dominated by the effects of rotation compared to advection
 64 (Rossby number : $Ro \ll 1$) and stratification compared to vertical shear (Richardson number
 65 : $Ri \gg 1$). Ageostrophic flows account for variations in the geostrophically balanced system.
 66 They are characterized by a large vertical component and the increasing effects of advection.

67 Mesoscale eddies are easily tracked by satellite altimetry, which measures sea surface
 68 height (η) and whose low-frequency component is an indirect measure of surface geostrophic
 69 currents. Satellite altimetry has shown that mesoscale eddies are ubiquitous in the oceans
 70 and that they are most energetic in western boundary currents and in the Antarctic Circum-
 71 polar Current (Ducet et al., 2000; Chelton et al., 2007, 2011). This identifies these regions
 72 as key to the global ocean energy budget.

73 Using satellite altimetry data, Zhai et al. (2010) suggested western boundaries as
 74 mesoscale eddy kinetic energy (EKE) sinks. In the energy budget, sources and sinks of
 75 eddy kinetic energy (EKE) are accounted for by the EKE flux divergence term (Harrison
 76 & Robinson, 1978). This term represents the rate of EKE transport done by: the work
 77 of pressure fluctuations (eddy pressure work; usually interpreted as the linear contribution
 78 from waves) and the nonlinear advection of EKE by mean and eddy flows. When ocean
 79 dynamics are in equilibrium, the EKE flux divergence indicates a net EKE source (>0) or
 80 sink (<0).

81 Zhai et al. (2010) explicitly developed a η -based diagnostic of the mesoscale eddy pres-
 82 sure work (linear component of the EKE flux divergence) using several approximations.
 83 Their diagnosis reduces to the linear contribution of the β -effect, corresponding in particu-
 84 lar to the propagation of long Rossby waves. Figure 1a shows Zhai et al. (2010)'s version
 85 of the eddy pressure work in the Agulhas Current region, which they suggested to be the
 86 largest mesoscale EKE sink. The approximated η -based eddy pressure work indicates an
 87 almost uniform mesoscale EKE sink (<0) at the western boundary (WB; black domain),
 88 whose cumulative value is of $O(1)$ GW (Figure 1a).

89 Their result would establish the following paradigm: mesoscale eddies originate almost
 90 everywhere in the ocean, propagate westward at about the speed of long baroclinic Rossby
 91 waves, and decay at western boundaries, probably through direct energy routes to dissipa-
 92 tion, channeled by topography (Gill et al., 1974; Zhai et al., 2010; Chelton et al., 2011;
 93 Evans et al., 2022). This scenario is supported in regions free of western boundary currents,
 94 by *in situ* measurements and idealized numerical simulations (Evans et al., 2020; Z. Yang
 95 et al., 2021; Evans et al., 2022). However, in regions containing western boundary currents,
 96 model-based studies suggest more complex mesoscale eddy dynamics. Western boundaries
 97 are hotspots for mesoscale eddy generation due to instabilities of the western boundary
 98 currents (Halo et al., 2014; Kang & Curchitser, 2015; Gula et al., 2015; Y. Yang & Liang,
 99 2016; Yan et al., 2019; Li et al., 2021; Jamet et al., 2021; Tedesco et al., 2022).

100 In particular, a recent study has shown that the Agulhas Current region is a mesoscale
 101 EKE source using an unapproximated EKE flux divergence performed from a model
 102 (Tedesco et al., 2022). Figure 1d,e shows the unapproximated eddy pressure work and ad-
 103 vection of EKE (forming the EKE flux divergence) computed from 3-dimensional modeled
 104 mesoscale velocities (Tedesco et al., 2022). Both unapproximated terms differ significantly
 105 from the approximated η -based eddy pressure work, with their magnitudes being larger of
 106 an order and their scale patterns smaller (Figure 1d,e). In the WB region of the Agulhas

107 Current, the two unapproximated terms are the most intense on the shelf — over a band
 108 narrower than the WB width — and have locally comparable magnitudes. Their cumulative
 109 value represents a mesoscale *EKE* source (>0), whose main contribution is due to the
 110 advection of *EKE*.

111 The opposite mesoscale *EKE* sources and sinks supported in the Agulhas Current
 112 region by the different versions of the *EKE* flux divergence (Figure 1a,d,e reproducing Zhai
 113 et al., 2010; Tedesco et al., 2022), challenge (1) the hypothesis that long baroclinic Rossby
 114 waves are the main contributors to the mesoscale *EKE* flux divergence, and thus (2) the
 115 approximations used to derive the η -based term. In this study, we focus on explaining the
 116 differences between the approximated η -based and the unapproximated model-based *EKE*
 117 flux divergence in the Agulhas Current region. We discuss below the approximations used
 118 by Zhai et al. (2010) and their implications:

119 (i) **Mesoscale *EKE* flux divergence is mainly due to geostrophic flows**

120 The geostrophic approximation is required when using satellite altimetry data. Geostro-
 121 phy is a good approximation to infer mesoscale eddy velocities, which have small
 122 Rossby numbers ($Ro = O(\ll 0.05)$; Chelton et al., 2011). However, the use of
 123 geostrophic velocities to infer the mesoscale *EKE* flux divergence — a tendency term
 124 of the *EKE* budget that represents the rate of spatial redistribution of the mesoscale
 125 *EKE* reservoir (Harrison & Robinson, 1978) — is a separate issue.

126 (ii) **The vertical structure of mesoscale eddies is represented by the 1st baro-
 127 clinic mode**

128 The sea surface height (η) is usually interpreted as primarily reflecting surface-
 129 intensified vertical structures represented by the 1st baroclinic mode. However, the
 130 mesoscale *EKE* reservoir is represented by the combination of the barotropic and 1st
 131 baroclinic modes (Wunsch, 1997; Smith & Vallis, 2001; Venaille et al., 2011). The par-
 132 titioning between the two vertical modes varies regionally, from being close to equipar-
 133 tition to being dominated by one of the modes (Tedesco et al., 2022; Yankovsky et al.,
 134 2022). The contributions of the barotropic and 1st baroclinic modes to the mesoscale
 135 *EKE* flux divergence remain unknown to our knowledge. Their individual contribu-
 136 tions can possibly transport *EKE* in a decoupled (coupled) manner, which would
 137 then compensate (accumulate) when considering the *EKE* flux divergence for the
 138 mesoscale reservoir.

139 (iii) **Mesoscale *EKE* flux interactions with topography are weak**

140 The approximation of weak topographic interactions is equivalent to assuming that
 141 the mesoscale *EKE* flux has spatial variations larger than those of topography (Zhai
 142 et al., 2010). This approximation is challenged by (1) the large topographic gradients
 143 at western boundaries ($1 \cdot 10^{-2} \pm 2 \cdot 10^{-2}$ in the Agulhas Current region) and (2)
 144 the strong topographic control on mesoscale eddy dynamics at western boundaries.
 145 Topography controls the triggering of current instabilities that generate mesoscale
 146 eddies (Lutjeharms, 2006; Gula et al., 2015) and helps to channel energy transfers
 147 between mesoscale eddies and other types of flow (Adcock & Marshall, 2000; Nikurashin
 148 & Ferrari, 2010; Evans et al., 2020; Perfect et al., 2020; Tedesco et al., 2022). The
 149 contribution of topography to the mesoscale *EKE* flux divergence remains, to our
 150 knowledge, an open question.

151 In summary, opposing paradigms of mesoscale eddy dynamics are supported by two
 152 versions of the diagnosis of the *EKE* flux divergence in the western boundary region of
 153 the Agulhas Current (Zhai et al., 2010; Tedesco et al., 2022). The two diagnoses differ in
 154 method (η field measured by satellite altimetry vs. modeled 3-dimensional velocities) and
 155 assumed leading order contribution to the *EKE* flux divergence (long baroclinic Rossby
 156 waves as a result of approximations (i), (ii) and (iii) vs. no approximations to account for
 157 geostrophic, ageostrophic and topographic contributions acting on the barotropic and 1st
 158

160 baroclinic mode). The two contradictory diagnoses of mesoscale *EKE* source and sink suggest
161 that either the method or the approximations lead to a misestimation of the mesoscale
162 *EKE* flux divergence. This raises questions about the main contributions to the dynamics
163 of the mesoscale eddy energy reservoir, and consequently, about strategies for studying
164 mesoscale eddies. Open questions include: What are the main contributions – among
165 geostrophic and ageostrophic effects, barotropic and 1st baroclinic modes, and topographic
166 contribution – to the eddy pressure work and advection of *EKE*? What are the implications
167 for inferring the mesoscale *EKE* flux divergence using the η field? We focus in particular on
168 determining whether approximation (i) of geostrophy is valid, as it is the only one formally
169 required for the use of satellite altimetry to infer the mesoscale *EKE* flux divergence.

170 In the present study, we use a numerical simulation to evaluate the validity of approxi-
171 mation (i) for inferring the mesoscale *EKE* flux divergence in the region of the Agulhas
172 Current. Our study is organized as follows. Unapproximated and η -based expressions of
173 the eddy pressure work and advection of *EKE* (which form the *EKE* flux divergence) are
174 presented in section 2. The regional numerical simulation is presented in section 3. The
175 unapproximated and η -based versions of the eddy pressure work and advection of *EKE* are
176 evaluated in sections 4, 5 and 6. Finally, we discuss our results in the larger context of
177 altimetry-based diagnosis of mesoscale eddy dynamics at western boundaries in section 7.

2 Theory

In this section we present the modal *EKE* flux divergence. First, we present the theoretical framework of the vertical modes. Then, we define the unapproximated expression of the modal *EKE* flux divergence, which consists of the eddy pressure work (*EPW*) and the advection of *EKE* (*AEKE*). Finally, we define the η -based expressions of *EPW* and *AEKE*.

2.1 Vertical modes

A convenient approach to describe the vertical structure of mesoscale motions is the modal decomposition using traditional vertical modes (Gill, 1982). The vertical structure of the mesoscale *EKE* reservoir corresponds to the combination of the barotropic and 1st baroclinic modes (Wunsch, 1997; Smith & Vallis, 2001; Venaille et al., 2011; Tedesco et al., 2022), which represents surface-intensified vertical structures energised to the bottom.

The vertical modes ϕ_n for the horizontal velocity (\mathbf{u}) and the dynamical pressure (p) are the eigenfunctions solution of the Sturm-Liouville problem (Eq. 1), using linearized free-surface ($(\frac{\partial}{\partial z}\phi_n|_{z=\eta} = \frac{-N^2}{g}\phi_n|_{z=\eta})$) and flat-bottom boundary conditions ($(\frac{\partial}{\partial z}\phi_n|_{z=-H} = 0)$)
 \vdots

$$\frac{\partial}{\partial z} \left(\frac{1}{N^2} \frac{\partial}{\partial z} \phi_n \right) + \frac{1}{c_n^2} \phi_n = 0 \quad (1)$$

with N^2 the time-averaged buoyancy frequency, g the acceleration of gravity and $c_n^2 = \frac{1}{n\pi} \int_{-H}^{\eta} N(\mathbf{x}, z) dz$ the eigenvalues of the vertical modes.

The modal base ϕ_n satisfies the orthogonality condition :

$$\int_{-H}^{\eta} \phi_m \phi_n \ dz = \delta_{mn} h \quad (2)$$

with δ_{mn} the usual Kronecker symbol and $h = \eta + H$ the water column depth.

The dynamical variables are projected onto n vertical modes as follows :

$$[\mathbf{u}_n(\mathbf{x}, t), \frac{1}{\rho_0} p_n(\mathbf{x}, t)] = \frac{1}{h} \int_{-H}^{\eta} [\mathbf{u}(\mathbf{x}, z, t), \frac{1}{\rho_0} p(\mathbf{x}, z, t)] \phi_n(\mathbf{x}, z) dz \quad (3)$$

with \mathbf{u}_n and p_n the modal amplitudes of the horizontal velocity (\mathbf{u}) and dynamical pressure (p) and ρ_0 the reference density value.

The vertical modes are related to horizontal scales via c_n^2 , which are good approximations of the Rossby baroclinic deformation radii : $Rd_{n \geq 1} = \frac{c_n}{|f|}$ (Chelton et al., 1998), with f the Coriolis parameter.

2.2 Unapproximated modal *EKE* flux divergence

2.2.1 EKE flux divergence in the EKE budget

The modal EKE flux divergence is a term of the modal EKE budget. A comprehensive modal EKE budget has been derived in Tedesco et al. (2022), inspired from the budget derived in the context of internal tides (Kelly, 2016). The modal EKE budget reads as follows:

$$\begin{aligned}
& \underbrace{\mathbf{u}'_n \cdot (\rho_0 h \frac{\partial}{\partial t} \mathbf{u}'_n)}_{Time\ rate} + \underbrace{\nabla_H \cdot \int_{-H}^H \mathbf{u}'_n p'_n \phi_n^2 dz}_{Eddy-pressure\ work\ (EPW)} + \underbrace{\frac{\rho_0}{2} \nabla_H \cdot \int_{-H}^H \mathbf{u}_n \phi_n \|\mathbf{u}'_n \phi_n\|^2 dz}_{Advection\ of\ EKE\ (AEKE)} \\
& \qquad \qquad \qquad EKE\ flux\ divergence\ (EPW+AEKE) \\
& = \sum \left(\underbrace{S_n}_{EKE\ sources} + \underbrace{D_n}_{EKE\ sinks} \right)
\end{aligned} \tag{4}$$

198 Terms are time-averaged and the primes indicate fluctuations relative to the time-average.
 199 The dynamical pressure ($p(\mathbf{x}, z, t)$) is derived from the *in situ* density ($\rho(\mathbf{x}, z, t)$) from which
 200 the background density profile ($\bar{\rho}(z)$, defined as the spatial and temporal average of the *in*
 201 *situ* density) has been subtracted.

202 The *EKE* flux divergence corresponds to the rate of *EKE* spatial transport. When
 203 integrated over a domain, the *EKE* flux divergence corresponds to the transport across
 204 the domain boundaries. A positive (negative) sign indicates that outgoing (incoming) flux
 205 dominate the incoming (outgoing) flux. At equilibrium, the time rate of *EKE* (Eq. 4) is
 206 negligible. The *EKE* flux divergence is therefore equal to the sum of the *EKE* sources and
 207 sinks accounted for in the right-hand side of the modal *EKE* budget (S_n and D_n in Eq. 4).
 208 A positive (negative) *EKE* flux divergence thus represents a net *EKE* source (sink) that
 209 is then transported away (has been transported in).

210 The *EKE* flux divergence consists of two contributions: the eddy pressure work (*EPW*;
 211 Eq. 4) and the advection of *EKE* by the mean and eddy flows (*AEKE*; Eq. 4) (Harrison &
 212 Robinson, 1978). *EPW* is the only contribution to the *EKE* flux divergence in the context
 213 of linear theories of internal waves (Kelly et al., 2010, 2012; Kelly, 2016) and of Rossby waves
 214 (Masuda, 1978). It is also the main contribution for interior-ocean dynamics (Harrison &
 215 Robinson, 1978). *AEKE* can contribute significantly to the *EKE* flux divergence and can
 216 be equivalent to *EPW* in regions of high variability (Harrison & Robinson, 1978; Capó et
 217 al., 2019; Tedesco et al., 2022).

218 Here, we study the *EKE* flux divergence for the mesoscale reservoir over the period
 219 1995-2004. We define the mesoscale *EKE* flux divergence as the sum of the barotropic
 220 ($n = 0$) and 1st baroclinic ($n = 1$) contributions: $EPW_{n=0-1}$ and $AEKE_{n=0-1}$. To
 221 simplify notations, we refer to the mesoscale terms as *EPW* and *AEKE* in the following.
 222 The modeled mesoscale eddy dynamics over the period 1995-2004 is in equilibrium. The
 223 smallness of the time rate of *EKE* (Eq. 4) has been asserted for the period 1995-1999 in
 224 Tedesco et al. (2022). It is even smaller for the period 1995-2004 considered in this study.

225 2.2.2 Contributions to the *EKE* flux divergence

EPW and *AEKE* (Eq. 4) can be written as the sum of the contributions of *EKE* flux
 ($A + B$ in Eq. 5, 6) and *EKE* flux interacting with topographic gradients (C in Eq. 5, 6)
 as follows:

$$EPW = \underbrace{\int_{-H}^{\eta} p'_n \phi_n \nabla_H \cdot (\mathbf{u}'_n \phi_n) dz}_{\text{velocity divergence (A)}} + \underbrace{\int_{-H}^{\eta} (\mathbf{u}'_n \phi_n) \cdot \nabla_H (p'_n \phi_n) dz}_{\text{work of eddy pressure shear (B)}} \quad (5)$$

$$+ \underbrace{\nabla_H \eta \cdot |\mathbf{u}'_n p'_n \phi_n|^2|_{z=\eta} + \nabla_H H \cdot |\mathbf{u}'_n p'_n \phi_n|^2|_{z=-H}}_{\text{topographic-contribution (C)}}$$

$$AEKE = \underbrace{\frac{\rho_0}{2} \int_{-H}^{\eta} \|\mathbf{u}'_n \phi_n\|^2 \nabla_H \cdot (\mathbf{u}_n \phi_n) dz}_{\text{velocity divergence (A)}} + \underbrace{\frac{\rho_0}{2} \int_{-H}^{\eta} (\mathbf{u}_n \phi_n) \cdot \nabla_H \|\mathbf{u}'_n \phi_n\|^2 dz}_{\text{work of EKE shear (B)}} \quad (6)$$

$$+ \underbrace{\frac{\rho_0}{2} \nabla_H \eta \cdot |\mathbf{u}_n \phi_n||\mathbf{u}'_n \phi_n||^2|_{z=\eta} + \frac{\rho_0}{2} \nabla_H H \cdot |\mathbf{u}_n \phi_n||\mathbf{u}'_n \phi_n||^2|_{z=-H}}_{\text{topographic-contribution (C)}}$$

226 The *EKE* flux term ($A + B$; Eq. 5, 6) consists of a velocity divergence contribution
 227 (A) and an eddy pressure shear work for *EPW* (B in Eq. 5) and an *EKE* shear work
 228 for *AEKE* (B in Eq. 6). From their analytical expressions, it can be deduced that the

importance of geostrophic and ageostrophic effects varies between A and B . The velocity divergence contributions (A) mainly account for ageostrophic effects, since geostrophic velocities are horizontally divergent-free. The only geostrophic effects in A are due to geostrophic velocities expressed in the β -plane (Cushman-Roisin & Beckers, 2011). The geostrophic A -contributions acting on EPW and $AEKE$ are thus reduced to EKE flux driven by the β -effect. In the case of EPW (Eq. 5), the β -driven linear EKE flux corresponds to long baroclinic Rossby waves and was assumed by Zhai et al. (2010) to be the primary contributor to EPW , and subsequently to the EKE flux divergence. The work contribution (B) accounts for geostrophic and ageostrophic effects in different proportions for EPW and $AEKE$. For EPW (Eq. 5), the B -contribution is exclusively due to ageostrophic effects. Indeed, geostrophic velocities are orthogonal to the eddy pressure shear resulting in the cancellation of the eddy pressure shear work. For $AEKE$ (Eq. 6), the B -contribution accounts for both geostrophic and ageostrophic effects. Geostrophic velocities are in the same direction than the EKE shear, resulting in a non-null work.

The topographic-contribution (C ; Eq. 5,6) acting on EPW and $AEKE$ represents the interactions of EKE flux with topography and sea surface height gradients. It can be reduced to the contribution of topography gradients, which are much larger than η gradients ($||\nabla_H \eta|| = O(10^{-4}) ||\nabla_H H||$). The analytical expression of C does not allow the contribution of geostrophic or ageostrophic effects to be readily separated.

2.3 Approximated η -based modal EKE flux divergence

In the following, we present the η -based expressions of EPW and $AEKE$ accounting for approximation (i). We also present two other η -based expressions of EPW accounting for approximations (ii) and (iii). The main expressions of EPW and $AEKE$ discussed in this study are listed in Tables 1 and 2.

2.3.1 Approximations (i) of geostrophic velocities ($EPW_{(i)}$ and $AEKE_{(i)}$)

Approximation (i) of geostrophy is required by the use of η to infer the EKE flux divergence. EPW and $AEKE$ are written as $EPW_{(i)}$ and $AEKE_{(i)}$ when using modal geostrophic velocities (Table 1, 2). Modal geostrophic velocities are expressed from η fields, modulated to account for the fraction of the different vertical modes with $\lambda_n = \frac{\eta_n}{\eta}$ and $\alpha_n = \frac{\eta'_n}{\eta'}$, as follows:

$$\mathbf{u}_{g,n} \phi_n = \mathbf{k} \wedge \frac{g}{f} \nabla_H \left(\frac{\phi_n}{|\phi_n|_{z=0}} \lambda_n \eta \right) \quad (7)$$

$$\mathbf{u}'_{g,n} \phi_n = \mathbf{k} \wedge \frac{g}{f} \nabla_H \left(\frac{\phi_n}{|\phi_n|_{z=0}} \alpha_n \eta' \right) \quad (8)$$

Approximation (i) of geostrophy has a larger impact on EPW than on $AEKE$. $EPW_{(i)}$ (Table 1) reduces to a linear EKE flux driven by the β -effect ($A1$) and two topographic contributions, one acting on the β -driven EKE flux ($A2$) and the other acting on geostrophic EKE flux (C). $AEKE_{(i)}$ (Table 2) includes the β -effect (A), the geostrophic EKE shear work (B) and a topographic contribution acting on the geostrophic EKE flux (C).

2.3.2 Approximations (ii) and (iii) ($EPW_{(i,ii)}$ and $EPW_{(i,ii,iii)}$)

The η -based version of EPW defined by Zhai et al. (2010) relies on the additional approximations (ii) and (iii), which are not formally required by the use of η to infer the EKE flux divergence. Approximations (ii) and (iii) therefore lead to approximated versions of the η -based EPW : $EPW_{(i,ii)}$ and $EPW_{(i,ii,iii)}$ (Table 1).

Table 1: Summary of the unapproximated and η -based versions of the eddy pressure work (EPW).

Acronyms	Analytical expressions	Descriptions
EPW	$\underbrace{\nabla_H \cdot \int_{-H}^{\eta} \mathbf{u}'_n p'_n \phi_n^2 dz}_{(A+B+C)}$	unapproximated mesoscale eddy pressure work
$EPW_{(i)}$	$\underbrace{-\frac{\beta \rho_0 g^2}{2f^2} \frac{\partial}{\partial x} \left(\frac{\int_{-H}^{\eta} \phi_n^2 dz}{ \phi_n^2 _{z=0}} \alpha_n^2 \eta'^2 \right)}_{\beta\text{-contribution (A1)}} + \underbrace{\frac{\beta \rho_0 g^2}{2f^2} \frac{\partial H}{\partial x} \frac{ \phi_n^2 _{z=-H} \alpha_n^2 \eta'^2}{ \phi_n^2 _{z=0}}}_{\beta\text{-driven topographic-contribution (A2)}}$ $+ \frac{\rho_0 g^2}{2f} \nabla_H H \cdot \mathbf{k} \wedge \nabla_H \left(\frac{ \phi_n^2 _{z=-H} \alpha_n^2 \eta'^2}{ \phi_n^2 _{z=0}} \right), \text{ with } \alpha_n = \frac{\eta'}{\eta}$	unapproximated η -based version of mesoscale eddy pressure work (use of approximation (i))
$EPW_{(i,ii)}$	$\underbrace{-\frac{\beta \rho_0 g^2}{2f^2} \frac{\partial}{\partial x} \left(\frac{\int_{-H}^{\eta} \phi_1^2 dz}{ \phi_1^2 _{z=0}} \eta'^2 \right)}_{\beta\text{-contribution (A1)}} + \underbrace{\frac{\beta \rho_0 g^2}{2f^2} \frac{\partial H}{\partial x} \frac{ \phi_1^2 _{z=-H} \eta'^2}{ \phi_1^2 _{z=0}}}_{\beta\text{-driven topographic-contribution (A2)}}$ $+ \frac{\rho_0 g^2}{2f} \nabla_H H \cdot \mathbf{k} \wedge \nabla_H \left(\frac{ \phi_1^2 _{z=-H} \eta'^2}{ \phi_1^2 _{z=0}} \right)$	approximated η -based version of mesoscale eddy pressure work (use of approximations (i) and (ii))
$EPW_{(i,ii,iii)}$	$\underbrace{-\frac{\beta \rho_0 g^2}{2f^2} \frac{\partial}{\partial x} \left(\frac{\int_{-H}^{\eta} \phi_1^2 dz}{ \phi_1^2 _{z=0}} \eta'^2 \right)}_{\beta\text{-contribution (A1)}}$	approximated η -based version of mesoscale eddy pressure work defined by Zhai et al. (2010) (use of approximations (i), (ii) and (iii))

Table 2: Summary of the unapproximated and η -based versions of the advection of mesoscale EKE (AEKE).

Acronyms	Analytical expressions	Descriptions
$AEKE$	$\frac{\rho_0}{2} \nabla_H \cdot \underbrace{\int_{-H}^{\eta} \mathbf{u}_n \phi_n \mathbf{u}'_n \phi_n ^2 dz}_{(A+B+C)}$	unapproximated advection of mesoscale EKE
$AEKE_{(i)}$	$ \begin{aligned} & - \underbrace{\frac{\beta \rho_0 g}{2 f^2} \int_{-H}^{\eta} \mathbf{u}'_{g,n} \phi_n ^2 \frac{\partial}{\partial x} \left(\frac{\phi_n}{ \phi_n _{z=0}} \lambda_n \eta \right) dz + }_{velocity \ divergence \ (A)} \\ & \quad \underbrace{\frac{\rho_0}{2} \int_{-H}^{\eta} (\mathbf{u}_{g,n} \phi_n) \cdot \nabla_H \mathbf{u}'_{g,n} \phi_n ^2 dz}_{work \ of \ EKE \ shear \ (B)} \\ & + \underbrace{\frac{\rho_0}{2} \nabla_H H \cdot \mathbf{u}_{g,n} \phi_n \mathbf{u}'_{g,n} \phi_n ^2 _{z=-H}}_{topographic-contribution \ (C)} \end{aligned} $	unapproximated η -based version of advection of mesoscale EKE (use of approximation (i))

264 2.3.2.1 Approximation (ii) of sea surface height primarily reflecting the 1st baroclinic
 265 mode ($EPW_{(i,ii)}$)
 266

$EPW_{(i,ii)}$ is written as $EPW_{(i)}$, but assumes that modal geostrophic velocities expressed from η reflect only the 1st baroclinic mode (Table 1), using $\alpha_n \sim \alpha_1 \sim 1$, as follows:

$$\mathbf{u}'_{g,1}\phi_1 = \mathbf{k} \wedge \frac{g}{f} \nabla_H \left(\frac{\phi_1}{|\phi_1|_{z=0}} \eta' \right) \quad (9)$$

267 2.3.2.2 Approximation (iii) of weak topographic-contributions ($EPW_{(i,ii,iii)}$)
 268

$EPW_{(i,ii,iii)}$ (A1; Eq. 10) is derived from $EPW_{(i,ii)}$ ($A1 + A2 + C$), assuming that topographic contributions ($A2$ and C) are negligible:

$$EPW_{(i,ii,iii)} = \underbrace{-\frac{\beta \rho_0 g^2}{2f^2} \frac{\partial}{\partial x} \left(\frac{\int_{-H}^H \phi_1^2 dz}{|\phi_1^2|_{z=0}} \eta'^2 \right)}_{\beta\text{-contribution } (\mathbf{A1})} \quad (10)$$

269 $EPW_{(i,ii,iii)}$ (A1; Table 1) corresponds to a β -driven linear EKE flux acting on the
 270 1st baroclinic mode, which represents the contribution of long baroclinic Rossby waves to
 271 the EKE flux divergence. $EPW_{(i,ii,iii)}$ is the approximated η -based version of EPW used
 272 in Zhai et al. (2010), which established the paradigm of mesoscale eddies decay at western
 273 boundaries.

274 This study focuses on evaluating the main contributions to EPW and $AEKE$ (which
 275 form the EKE flux divergence) in the Agulhas Current region (Figure 1d,e). To do this, we
 276 evaluate the impacts of approximations (i), (ii) and (iii) on EPW and of approximation (i)
 277 on $AEKE$. We start our analysis by EPW , which is the term explicitly discussed in Zhai et
 278 al. (2010). We first evaluate the validity of approximations (ii) and (iii) to infer the η -based
 279 EPW (cf. section 4). This allows us to define $EPW_{(i)}$ — the unapproximated η -based
 280 EPW — which we then use to evaluate the validity of approximation (i) of geostrophy to
 281 infer the unapproximated EPW (cf. section 5). We next expand our analysis to $AEKE$
 282 (cf. section 6). This term dominates the cumulative value of the EKE flux divergence in
 283 the WB region (Figure 1e) and is not explicitly discussed in Zhai et al. (2010).

284 Evaluation of the effects of approximations (i), (ii) and (iii) on EPW provides information
 285 on the elements of mesoscale eddy dynamics that invalidate the paradigm of mesoscale
 286 eddy graveyard in the Agulhas Current region. In addition, evaluation of the effect of ap-
 287 proximation (i) of geostrophy on EPW and $AEKE$ provides information on the possibility
 288 of using η to infer EKE flux divergence.

289 **3 Method**

290 In this section, we present and evaluate the regional numerical simulation of the Agulhas
 291 Current. We first present the numerical set-up and observations used in this study. We
 292 then evaluate the modeled mesoscale eddy dynamics against observations. The modeled
 293 mesoscale *EKE* in the Agulhas Current region has already been evaluated against satellite
 294 altimetry data in Tedesco et al. (2022). Here, we evaluate the η -based version of *EKE* flux
 295 divergence defined by Zhai et al. (2010) ($EPW_{(i,ii,iii)}$) derived from our numerical simulation
 296 against one derived from observations. The computation of $EPW_{(i,ii,iii)}$ (A1; Table 1)
 297 requires the computation of vertical modes — based on the time-averaged stratification
 298 (N^2) — and η .

299 **3.1 Numerical model**

300 The regional numerical simulation of the Agulhas Current was performed using the
 301 Coastal and Regional COmmunity (CROCO) model. It is a free surface model, based
 302 on ROMS (Shchepetkin & McWilliams, 2005), which solves the primitive equations in the
 303 Boussinesq and hydrostatic approximations using a terrain following coordinate system (De-
 304 breu et al., 2012). The numerical simulation is presented in details in Tedesco et al. (2022).
 305 The simulation has a horizontal resolution of $dx \sim 2.5$ km and 60 vertical levels. It en-
 306 compasses the Agulhas Current region from its source (north of the Natal Bight at $27^\circ S$)
 307 to the Agulhas Retroflection (at $\sim 37^\circ S$), from where it becomes the Agulhas Return Cur-
 308 rent. Boundary conditions are supplied by two lower-resolution grids ($dx \sim 22.5$ km and
 309 7.5 km, respectively covering most of the South Indian Ocean and its western part).

310 Vertical modes are derived from the time-averaged stratification over the period 1995-
 311 2004, computed from the modeled daily-averaged temperature and salinity.

312 **3.2 Observations**

313 The WOCE (World Ocean Circulation Experiment) climatology provides *in situ* tem-
 314 perature and salinity fields at a global scale for monthly compositing means at the horizontal
 315 resolution of 1° (Gouretski & Koltermann, 2004).

316 Altimetric data are mapped on a regular $1/4^\circ$ -grid by AVISO (Archiving, Validation
 317 and Interpretation of Satellite Oceanographic data) and provide global scale η field for
 318 weekly compositing means. We focus on a subset of data over the Agulhas Current region
 319 ($15^\circ E - 34^\circ E$ and $27^\circ S - 40^\circ S$) for the period 1995-2004.
 320

321 **3.3 Observed and modeled mesoscale *EKE* sources and sinks from $EPW_{(i,ii,iii)}$**

322 Figure 1a-c shows $EPW_{(i,ii,iii)}$ (Table 1) in the Agulhas Current region calculated
 323 from observations and the model. Observed and modeled $EPW_{(i,ii,iii)}$ show patterns in
 324 fairly good agreement in the Agulhas Current region. $EPW_{(i,ii,iii)}$ is most intense at the
 325 Retroflection and along the Agulhas Return Current ($O(0.1-0.5)$ $W m^{-2}$), where it has
 326 patterns alternating positive and negative signs. It is less intense along the Agulhas Current
 327 and in the Subgyre ($O(0.01-0.1)$ $W m^{-2}$), where it has more uniform patterns.

328 We define the western boundary (WB) region as extending from north of the Natal
 329 Bight ($\sim 27^\circ S$) to the African tip ($\sim 37^\circ S$), over a typical width for a western boundary
 330 current of about 150 km (black region in Figure 1). In the WB region, $EPW_{(i,ii,iii)}$ is
 331 roughly uniformly negative, indicating an *EKE* sink of cumulative magnitude $O(1)$ GW.
 332 This is consistent with the *EKE* sink emphasised by Zhai et al. (2010) at the western
 333 boundary of the South Indian Ocean (poleward of $10^\circ S$).

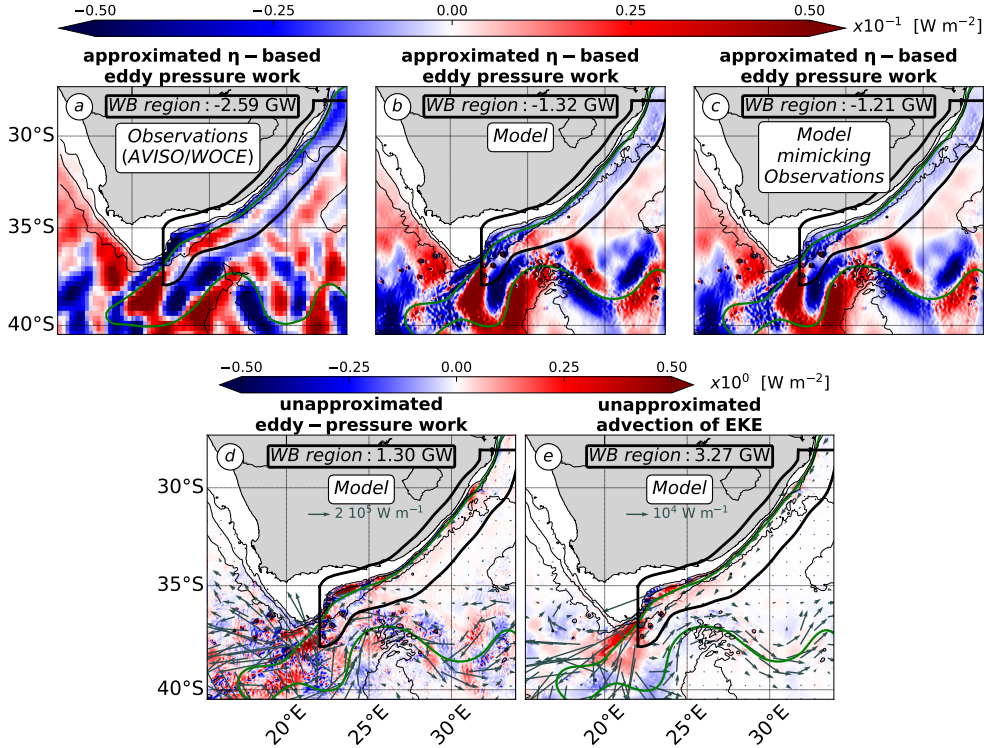


Figure 1: Different versions of the mesoscale EKE flux divergence (formed by eddy pressure work and advection of EKE) [W m^{-2}] in the Agulhas Current region. (a-c) Approximated η -based eddy pressure work performed from (a) observations (AVISO and WOCE data) following Zhai et al. (2010) and (b,c) a numerical simulation (built upon the CROCO model), at (b) the resolution of the simulation ($\text{dx} \sim 2.5 \text{ km}$) and (c) a coarsened resolution mimicking the resolution of observations. (d,e) Unapproximated model-based (d) eddy pressure work and (e) advection of EKE at the resolution of the simulation ($\text{dx} \sim 2.5 \text{ km}$). Note the different colorbar ranges between panels (a, b, c) and panels (d, e). Black area denotes the WB region. The cumulative terms in the WB region are in [GW] (10^9 W). Green contours denote the 0.25 m isoline of time-averaged η and black contours denote 1000 m and 3000 m isobaths.

Observed and modeled $EPW_{(i,ii,iii)}$ s differ mainly in the magnitude of the EKE sinks that they depict in the WB region. There is about a twofold decrease in the model compared to the observations (Figure 1a-c). The difference in magnitude is not explained by the coarser horizontal resolution of AVISO data (effective horizontal resolution of $O(100)$ km; Chelton et al., 2011) compared to the model (effective horizontal resolution of 25 km; following Soufflet et al., 2016). The twofold decrease in the model is also present when using smoothed modeled η , with a length scale of 100 km to mimic the altimetry data processing done by AVISO (Figure 1c). This indicates that the net EKE sink in the WB region is robust to altimetry data processing and that horizontal scales $< O(100)$ km do not contribute significantly to $EPW_{(i,ii,iii)}$. The difference in magnitude could be explained by too weak a forcing of remotely generated eddies in the model. The numerical simulation is forced at the boundaries by a parent simulation ($\text{dx} \sim 7.5 \text{ km}$), which resolves mesoscale eddies of scales 50 km–100 km, but underestimate their amplitude. See Appendix A for details of the evaluation of the amplitude of the modeled mesoscale eddy field against satellite altimetry

348 data. This underestimation in the model is likely due to a too weak inverse cascade at smaller
349 scales, which have been shown to substantially energize the mesoscale eddy energy reservoir
350 in the Agulhas Current region (Schubert et al., 2020). Note that the magnitude of the
351 cumulative *EKE* flux is sensitive to the definition of the WB region. Our definition of the
352 WB region best captures the *EKE* sink shown by the modeled and observed $EPW_{(i,ii,iii)}$.
353 However, the observed *EKE* sink extends further south of the WB region (Figure 1a), while
354 the modeled one is fully encompassed by the WB region — with its southern face closely
355 following the 0 W m^{-2} isoline — (Figure 1c,d).

356 The fairly good agreement between modeled and observed *EKE* reservoirs (Tedesco et
357 al., 2022) and $EPW_{(i,ii,iii)}$ (Figure 1a-c), indicates that our numerical simulation reliably
358 represents the mesoscale eddy dynamics, at least as inferred from satellite altimetry data.
359 Our numerical simulation is therefore suitable to evaluate the leading order contribution
360 of the *EKE* flux divergence, and subsequently to explain the opposing paradigms between
361 η -based and unapproximated diagnoses in this region.

362 **4 Approximated and unapproximated η -based EPWs ($EPW_{(i,ii,iii)}$ and
363 $EPW_{(i)}$)**

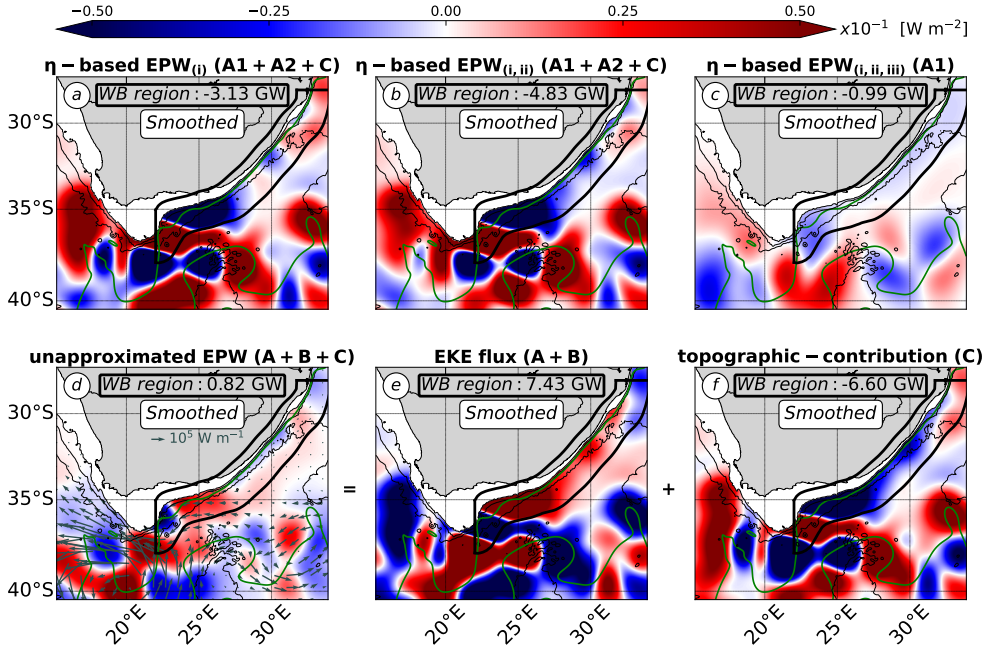


Figure 2: η -based and unapproximated EPWs [W m^{-2}] (Table 1). (a-c) Versions of η -based EPW, including (a) $EPW_{(i)}$, (b) $EPW_{(i,ii)}$, and (c) $EPW_{(i,ii,iii)}$. (d) Unapproximated EPW ($A+B+C$) split into the contributions of (e) EKE flux ($A+B$) and (c) topographic-contribution (C). Terms are smoothed with a 75 km-radius Gaussian kernel. (cf. Figure 1 for a detailed caption).

In this section, we evaluate the validity of approximations (ii) and (iii) to reliably infer the η -based $EPW_{(i)}$. We first compare $EPW_{(i)}$ (unapproximated η -based EPW) and $EPW_{(i,ii,iii)}$ (approximated η -based EPW used by Zhai et al., 2010). Next, we detail separately the differences due to approximations (ii) and (iii).

Note that most of the figures discussed in the study show smoothed terms (Figures 2, 4, B1). Smoothed terms highlight the large-scale patterns driving the cumulative contributions in the WB region. Smoothing also facilitates comparison between $EPW_{(i,ii,iii)}$ (Figure 1a-c) and the other EPW versions. The smoothing length scale corresponds to a typical mesoscale eddy radius at mid-latitudes (75 km), as inferred from satellite altimetry (Chelton et al., 2011). See Appendix B for details on the sensitivity of EPW to the smoothing length scale.

374 **4.1 Mesoscale EKE sources and sinks from the unapproximated and ap-
375 proximated η -based EPWs ($EPW_{(i)}$ vs. $EPW_{(i,ii,iii)}$)**

376 Figure 2a-c shows the different versions of the η -based EPW in the Agulhas Current
377 region ($EPW_{(i)}$, $EPW_{(i,ii)}$ and $EPW_{(i,ii,iii)}$). $EPW_{(i)}$ and $EPW_{(i,ii,iii)}$ have different
378 local patterns and magnitudes in the Agulhas Current region (Figure 2a,c). In the WB
379 region, $EPW_{(i)}$ is predominantly negative, but shows patterns of varying magnitude and sign
380 (Figure 2a). This contrasts with $EPW_{(i,ii,iii)}$ which is almost uniformly negative (Figure

381 Both EPWs show an EKE sink in the WB region, but that of $EPW_{(i)}$ (-3.13 GW) is
 382 significantly larger than that of $EPW_{(i,ii,iii)}$ (-0.99 GW).

383 The differences between $EPW_{(i)}$ and $EPW_{(i,ii,iii)}$ show that $EPW_{(i,ii,iii)}$ — the ap-
 384 proximated η -based version of EPW defined by Zhai et al. (2010) — is not a good estimate
 385 of the unapproximated η -based $EPW_{(i)}$ in the Agulhas Current region (Figure 2a,c). This
 386 indicates that one or both of the approximations (ii) and (iii) are not valid for inferring the
 387 η -based $EPW_{(i)}$.

388 4.2 Bias due to approximation (ii)

389 Approximation (ii) of η primarily reflecting the 1st baroclinic mode can bias the η -
 390 based $EPW_{(i,ii)}$ in two ways. It can bias the accurate estimate of the contribution of the
 391 1st baroclinic mode to the η -based $EPW_{(i)}$. η does not exclusively reflect eddies (η variance)
 392 of the 1st baroclinic mode. In the WB region of the Agulhas Current, the variance of the
 393 modeled η accounts for about 16 ± 4% of the barotropic mode, 38 ± 4% of the 1st baroclinic
 394 mode and 36 ± 2% of a coupling between the first 10 vertical modes (Figure C1). See
 395 Appendix C for details on the partitioning of the η variance into the 10 first vertical modes
 396 in the Agulhas Current region. Approximation (ii) may also bias the estimate of the EKE
 397 flux divergence for the mesoscale reservoir, because $EPW_{(i,ii)}$ does not include the barotropic
 398 contribution. Contributions from the barotropic and 1st baroclinic $EPW_{(i)}$ s can transport
 399 EKE in a decoupled (coupled) manner, which would then compensate (accumulate) when
 400 considering the EKE flux divergence for the mesoscale reservoir.

401 $EPW_{(i,ii)}$ and $EPW_{(i)}$ have similar local patterns and magnitudes in the Agulhas
 402 Current region (Figure 2a,b). However, their cumulative EKE sinks differ slightly in the
 403 WB region. $EPW_{(i,ii)}$ denotes a larger EKE sink (-4.83 GW; Figure 2b) than $EPW_{(i)}$
 404 (-3.13 GW; Figure 2a). $EPW_{(i,ii)}$ includes only the contribution from the 1st baroclinic
 405 mode, while $EPW_{(i)}$ can be split into the contributions of the barotropic mode (-1.01 GW
 406 in the WB region; not shown) and the 1st baroclinic mode (-2.12 GW in the WB region;
 407 not shown).

408 The large similarities between $EPW_{(i)}$ and $EPW_{(i,ii)}$ patterns (Figure 2a,b) indicate
 409 that approximation (ii) is not the main reason for the large discrepancies between $EPW_{(i)}$
 410 and $EPW_{(i,ii,iii)}$ in the Agulhas Current region (Figure 2a,c). However, approximation (ii)
 411 leads to an overestimation of (1) the EKE sink in the WB region (overestimation by 154%)
 412 and (2) the contribution of the 1st baroclinic mode (overestimation by 228%).

413 4.3 Bias due to approximation (iii)

414 The topography acts on $EPW_{(i,ii)}$ ($A_1 + A_2 + C$; Table 1) via two contributions:
 415 the β -driven flux (A_2) and the geostrophic EKE flux (C). Approximation (iii) of weak
 416 topographic contribution is equivalent to assuming that the mesoscale EKE flux (A_1) has
 417 larger spatial variations than that of the topography (A_2 and C) (Zhai et al., 2010).

418 $EPW_{(i,ii)}$ and $EPW_{(i,ii,iii)}$ have very different patterns and magnitudes in the Agulhas
 419 Current region (Figure 2b,c). These differences are the same as those for $EPW_{(i)}$ and
 420 $EPW_{(i,ii,iii)}$ (cf. section 4.1). This confirms that approximation (iii) is the one that limits
 421 the estimate of the η -based $EPW_{(i)}$ in the Agulhas Current region (Figures 2a,b,c). This
 422 also indicates that the topographic contributions (A_2 and C in $EPW_{(i)}$ and $EPW_{(i,ii)}$; Table
 423 1) dominate the η -based EPWs ($EPW_{(i)}$ and $EPW_{(i,ii)}$; Figures 2a,b). In particular, the
 424 topographic contribution to the geostrophic EKE flux (C : -4.54 GW in the WB region; not
 425 shown) is the dominant contribution, compared to the β -driven topographic contribution
 426 (A_2 : 0.70 GW in the WB region; not shown).

427 In summary, $EPW_{(i,ii,iii)}$ — the EPW version defined by Zhai et al. (2010) — is not a
 428 good estimate of $EPW_{(i)}$ — the unapproximated η -based EPW — in the Agulhas Current

429 region, because approximation (iii) is not valid (Figure 2a-c). In other words, the β -driven
430 linear *EKE* flux acting on the 1st baroclinic mode ($EPW_{(i,ii,iii)}$) is not the leading order
431 contribution to the η -based $EPW_{(i)}$. $EPW(i)$ ($A1 + A + 2 + C$; Figure 1a) is dominated by
432 interactions between the geostrophic *EKE* flux of the barotropic and 1st baroclinic modes
433 with topographic gradients (C).

434 However, the η -based $EPW_{(i)}$ still shows an *EKE* sink in the WB region (<0 ; Figure
435 2a) in contrast with the unapproximated EPW (>0 ; Figure 1d). This suggests that ap-
436 proximation (i) of geostrophy is the one at the origin of the opposing paradigms supported
437 by η -based and unapproximated EPW .

438 5 η -based $EPW_{(i)}$ and unapproximated EPW

439 In this section, we inform about the invalidity of approximation (i) of geostrophy for
 440 a reliable inference of the unapproximated EPW . We first evaluate the mesoscale EKE
 441 sources and sinks represented by the unapproximated EPW . We then characterize the main
 442 contributions to the unapproximated EPW .

443 5.1 Mesoscale EKE sources and sinks from the η -based $EPW_{(i)}$ and the 444 unapproximated EPW

445 $EPW_{(i)}$ and EPW show no similarity over the whole Agulhas Current region (Figure
 446 2a,d). In the WB region, they have similar patterns of locally opposite signs. These local
 447 differences are reflected in their cumulative values, which amount to an EKE sink (< 0) and an
 448 EKE source (> 0), for $EPW_{(i)}$ and EPW respectively. This confirms that
 449 approximation (i) of geostrophy is not valid for inferring EPW in the Agulhas Current
 450 region (Figure 2a,d).

451 The unapproximated EPW indicates a source of EKE in the WB region (0.82 GW;
 452 Figure 2d). The locally gained EKE is then exported downstream of the Agulhas Current,
 453 eventually towards the South Atlantic, or recirculated into the Indian Ocean along the
 454 Agulhas Return Current (vector field in Figure 2d). Locally, the unapproximated EPW
 455 shows patterns and magnitudes consistent with the documented variability of the Agulhas
 456 Current (Lutjeharms, 2006; Tedesco et al., 2022).

457 Along the northern branch of the WB region ($31^{\circ}\text{E} - 26^{\circ}\text{E}$), where the Agulhas Current
 458 is stable, the unapproximated EPW is weak compared to the rest of the domain and have
 459 patterns of contrasting sign (Figure 2d). EPW is negative upstream of the Natal Bight
 460 (31°E) and between the Natal Bight and the Agulhas Bank over a narrow band along the
 461 straight part of the shelf ($26^{\circ}\text{E}-30.5^{\circ}\text{E}$). In these areas, EPW (< 0) therefore indicates that
 462 the eddy dynamics are mainly acting to deplete the mesoscale reservoir. This is consistent
 463 with the northern Agulhas Current being stable due to the topographic constraint (Lut-
 464 jeharms, 2006; Tedesco et al., 2022). EPW is locally positive at the Natal Bight. This
 465 is consistent with the punctual generation (4–5 times per year) of Natal Pulses: mesoscale
 466 eddies that are the main source of variability of the Northern Agulhas Current (Lutjeharms,
 467 2006; Eliot & Beal, 2015).

468 Along the southern branch of the WB region ($26^{\circ}\text{E} - 23^{\circ}\text{E}$), where the shelf curvature
 469 increases and the Agulhas Current is unstable, the mesoscale EPW is large and positive
 470 (Figure 2d). In this area, EPW shows the largest EKE source of the WB region. This
 471 shows that eddy dynamics are mainly energising the mesoscale reservoir there. This is
 472 consistent with the highly unstable nature of the southern Agulhas Current and the doc-
 473 mented generation of quasi-permanent meanders there (Lutjeharms, Penven, & Roy, 2003;
 474 Lutjeharms, Boebel, & Rossby, 2003; Schubert et al., 2021). Note that the mesoscale EPW
 475 locally changes sign and becomes negative at the tip of the shelf ($24^{\circ}\text{E} - 23^{\circ}\text{E}$). There, the
 476 shelf curvature decreases and the current is constrained by the topography, locally enhancing
 477 EKE dissipation and preventing mixed barotropic-baroclinic instability to trigger (energy
 478 conversion terms of barotropic and baroclinic instability are negative, indicating a kinetic
 479 energy loss from mesoscale eddies in favor of the mean circulation; Tedesco et al., 2022).

480 5.2 Main contributions to the unapproximated EPW

481 Geostrophic effects are not the leading contribution to EPW in the Agulhas Current
 482 region. We therefore characterize the main contributions to the unapproximated mesoscale
 483 EPW below. We first evaluate the main contributions to the unapproximated EPW and
 484 then discuss their range of validity.

485 **5.2.1 Contributions of ageostrophic and topographic effects**

486 The unapproximated EPW ($A + B + C$; Table 1; Figure 2d) consists of an EKE
 487 flux contribution ($A + B$; Figure 2b) and a topographic contribution (C ; Figure 2c). Both
 488 are large and largely compensate in the Agulhas Current region. In the WB region, the
 489 cumulative value of EPW is dominated by the positive EKE flux contribution ($A + B$).
 490 However, it can be locally dominated by the negative topographic contribution (C), as for
 491 example along the straight part of the shelf, where a narrow band of negative EPW is
 492 visible ($30.5^{\circ}\text{E} - 26^{\circ}\text{E}$; Figure 2d).

493 The EKE flux contribution ($A + B$) and the topographic contribution (C) do not ac-
 494 count for geostrophic and ageostrophic effects to the same extent. Approximation (i) of
 495 geostrophy limits the estimate of the EKE flux contribution ($A + B$), because the unap-
 496 proximated $A + B$ (Figure 2e) is very different from its geostrophic analogue ($A1$; Figure
 497 2c). The velocity divergence contribution to the EKE flux (A) accounts for ageostrophic
 498 effects and the β -effect. While the eddy pressure shear work (B) exclusively accounts for
 499 ageostrophic effects (*cf.* section 2.2.2). The geostrophic EKE flux is thus reduced to a lin-
 500 ear β -effect ($A1$; Figure 2c), which we have shown to be negligible for the η -based $EPW_{(i)}$
 501 ($A1 + A2 + C$; Figure 2a).

502 On the other hand, approximation (i) of geostrophy allows to derive a qualitatively
 503 good estimate of the topographic contribution (C). The unapproximated C -contribution
 504 (Figure 2f) is similar to the η -based $EPW_{(i)}$ ($A1 + A2 + C$; Figure 2a), which we have seen
 505 to be dominated by the geostrophic C -contribution (*cf.* section 4).

506 Note that the EKE source shown by the unapproximated EPW in the WB region
 507 (0.82 GW; Figure 2d) is mainly due to the barotropic EPW (1.56 GW; not shown), while
 508 the 1^{st} baroclinic EPW represents an EKE sink (-0.74 GW; not shown) and acts against the
 509 barotropic EPW . This emphasises the importance of properly defining the unapproximated
 510 mesoscale EPW as the sum of barotropic and 1^{st} baroclinic $EPWs$. In the case of the
 511 unapproximated EPW , both vertical modes compensate each other, while in the case of
 512 the η -based $EPW_{(i)}$, both vertical modes amplify each other (*cf.* section 4). The different
 513 contributions of barotropic and 1^{st} baroclinic modes to the different versions of EPW is
 514 therefore non-trivial.

515 In summary, the η -based $EPW_{(i)}$ and the unapproximated EPW support opposite
 516 paradigms in the Agulhas Current region, because they have different leading order contribu-
 517 tions. We first showed that the η -based $EPW_{(i)}$ is dominated by the topographic con-
 518 tribution acting on the geostrophic EKE flux. We then showed that the unapproximated
 519 EPW is dominated overall by ageostrophic effects and locally by the topographic contribu-
 520 tion. In the following section, we characterize the range of validity for the dominance of
 521 ageostrophic effects.

522 **5.2.2 Scale analysis argument for large ageostrophic effects and weak β -
523 effect**

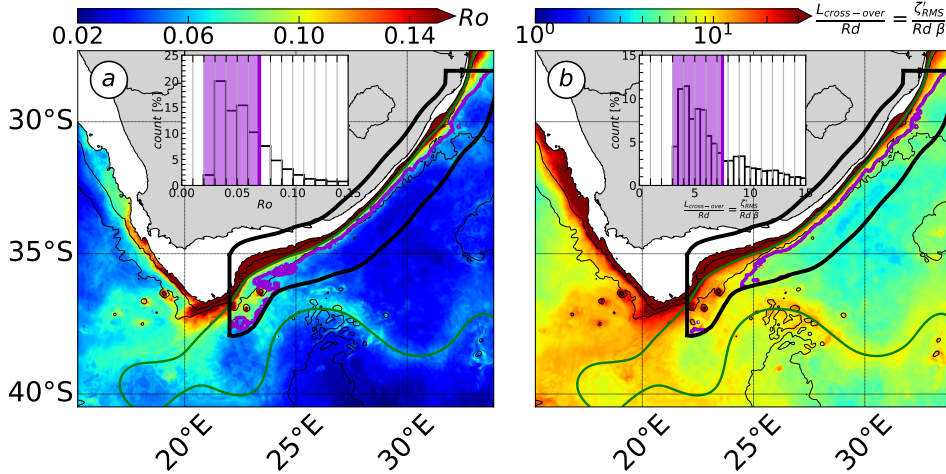


Figure 3: Adimensional metrics measuring the contribution of ageostrophic effects to EPW . (a) Rossby number for mesoscale eddies ($Ro = \frac{\zeta_{RMS}}{f}$) and (b) ratio between the cross-over scale ($L_{g,ag} = \frac{\zeta'}{\beta}$; Eq. 15) and the characteristics length scale of mesoscale eddies (Rossby deformation radius; Rd). In the barplots, counts of (a) and (b) in the WB region are expressed in [%] and shaded areas show the 70 % percentile. In the maps, purple contours show (a) and (b) 70 % percentiles in the physical space. (cf. Figure 1 for a detailed caption)

524 **5.2.2.1 Definition of a cross-over scale**
525

526 The founding hypothesis of the paradigm of mesoscale eddies graveyard at western
527 boundaries was that long baroclinic Rossby waves are the main contributor to the EKE
528 flux divergence (Zhai et al., 2010). This hypothesis favours one contribution of EPW —
529 the β -effect ($A1$ in $EPW_{(i)}$; Table 1) — over others, which include ageostrophic effects and
530 the topographic contribution. We have seen that for the EKE flux contribution ($A + B$)
531 acting on the unapproximated EPW (Table 1), ageostrophic effects overcome the β -effect
532 in the WB region of the Agulhas Current (cf. section 5). Here, we use a scale analysis to
533 evaluate in which regimes we can expect ageostrophic effects to dominate over the β -effect
534 for the unapproximated EPW .

535 Ageostrophic effects acting on the EKE flux contribution ($A+B$; Table 1) take the form
536 either of (1) both ageostrophic velocities and pressure ($EPW_{(ag)}$) or (2) coupled ageostrophic
537 velocities to geostrophic pressure ($EPW_{(g,ag)}$). Using quasi-geostrophic scalings of velocity
538 and pressure, we perform the scaling of $EPW_{(ag)}$ (Eq. 11), $EPW_{(g,ag)}$ (Eq. 12), and of the
539 β -effect (Eq. 13), as follows:

$$\left| \int_{-H}^{\eta} \nabla_H \cdot (\mathbf{u}'_{ag,n} p'_{ag,n} \phi_n^2) dz \right| \sim \frac{Ro^2 U'_g P'_g H}{L} \quad (11)$$

$$\left| \int_{-H}^{\eta} \nabla_H \cdot (\mathbf{u}'_{ag,n} p'_{g,n} \phi_n^2) dz \right| \sim \frac{Ro U'_g P'_g H}{L} \quad (12)$$

$$\left| \frac{\beta \rho_0 g^2}{2f^2} \int_H^{\eta} \frac{\partial}{\partial x} \left(\frac{\phi_n^2}{|\phi_n^2|_{z=0}} \alpha_n^2 \eta'^2 \right) dz \right| \sim \frac{\widehat{\beta} P' U'_g H}{\widehat{f}} \quad (13)$$

We use the following adimensionalized variables $|\nabla_H, \frac{\partial}{\partial x}| \sim \frac{1}{L}$, $\left| \int_{-H}^{\eta} < . > dz \right| \sim H$, $|\beta| \sim \widehat{\beta}$, $|f| \sim \widehat{f}$. Using the expansion of velocity and eddy pressure with Ro the small parameter, we define $|\mathbf{u}'_{ag,n}| \sim Ro U'_g$ and $|p'_{ag,n}| \sim Ro P'_g$, with $Ro = \left| \frac{1}{H} \int_{-H}^{\eta} \left(\frac{\zeta'_{RMS}}{f} \right) dz \right| \sim \frac{\widehat{\zeta'_{RMS}}}{\widehat{f}}$ the vertical average of the root mean square of the normalized relative vorticity for mesoscale eddies ($\zeta' = \partial_x v' - \partial_y u'$). Using geostrophy, we define $|p'_{g,n}| \sim P'_g \sim \rho_0 \widehat{f} U'_g L$. Using the hydrostatic approximation and geostrophy, we define $\left| \frac{\phi_n^2 \alpha_n^2 \eta'^2}{|\phi_n^2|_{z=0}} \right| \sim \frac{P'_g U'_g L \widehat{f}}{\rho_0 g^2}$.

The scale analysis is used to define two cross-over scales ($L_{g,ag}$ in Eq. 15 and L_{ag} in Eq. 14), at which the contributions to EPW of the two forms of ageostrophic EKE flux ($EPW_{(g,ag)}$ and $EPW_{(ag)}$) have the same order of magnitude as the contribution of the β -effect:

$$\frac{(11)}{(13)} = \frac{Ro^2 \widehat{f}}{L \widehat{\beta}} = \frac{\widehat{\zeta'_{RMS}}^2}{L \widehat{f} \widehat{\beta}} = \frac{L_{ag}}{L}, \text{ with } L_{ag} = \frac{\widehat{\zeta'_{RMS}}^2}{\widehat{f} \widehat{\beta}} \quad (14)$$

$$\frac{(12)}{(13)} = \frac{Ro \widehat{f}}{L \widehat{\beta}} = \frac{\widehat{\zeta'_{RMS}}}{L \widehat{\beta}} = \frac{L_{g,ag}}{L}, \text{ with } L_{g,ag} = \frac{\widehat{\zeta'_{RMS}}}{\widehat{\beta}} \quad (15)$$

$L_{g,ag}$ is the ratio of the eddy vorticity and of the β parameter (Eq. 15). $L_{g,ag}$ is greater than L_{ag} if the eddy Rossby number is < 1 , which is the case for mesoscale eddies. $L_{g,ag}$ will thus generally impose the most restrictive condition. Note that the definition of the cross-over scales is not unique. An equivalent definition involving the Rhines scale can be defined using another scaling of the eddy Rossby number ($Ro = \frac{U'}{fL}$). See appendix D for details on the alternative definition of $L_{g,ag}$ for the mesoscale EPW in the Agulhas Current region.

5.2.2.2 Cross-over scale performed in the Agulhas Current region

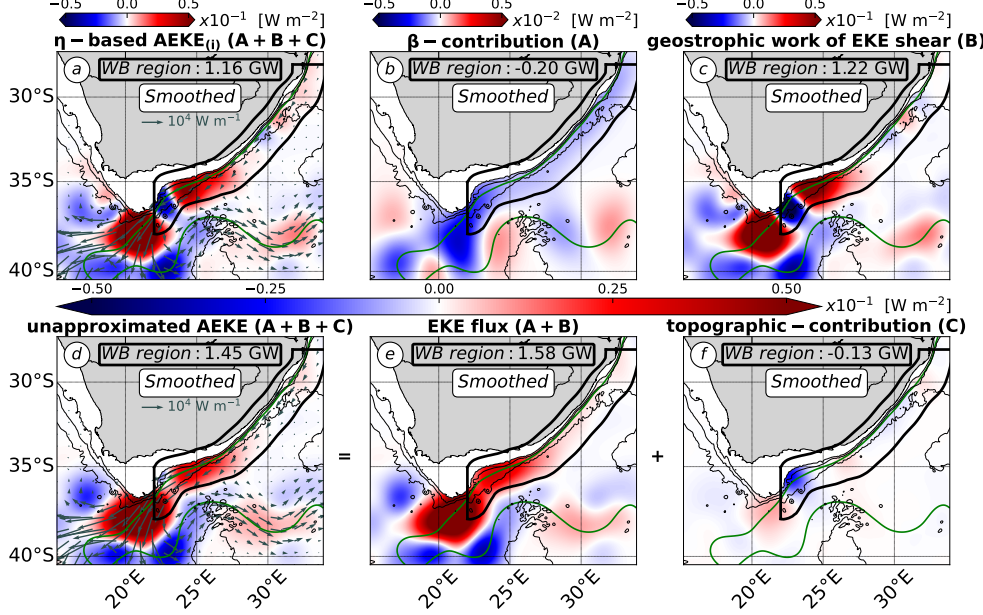
We compare $L_{g,ag}$ (Eq. 15) with the characteristic length scale of mesoscale eddies — the Rossby deformation radius (Rd) of about 30 km in the region of the Agulhas Current — (Figure 3). The typical values of Ro confirm that mesoscale eddies are mainly geostrophic in the WB region (Ro in $O(0.02-0.07)$ in 70% of the WB region and Ro in $O(0.07-0.65)$ at the inner front; Figure 3a). However, the typical values of $L_{g,ag}$ show that coupled geostrophic-ageostrophic effects dominate over the β -effect at mesoscale ($L_{g,ag}$ in $O(3-7)Rd$ in 70% of the WB region and $L_{g,ag}$ in $O(7-19)Rd$ at the inner front; Figure 3b). On the other hand, the purely ageostrophic effects are weaker than the contribution of the β -effect (L_{ag} in $O(0.1-0.5)Rd$ in the WB region; not shown).

Typical values of $L_{g,ag}$ (Eq. 15) are about $O(105-256)$ km in the region of the Agulhas Current (not shown). This sets the upper limit of the scale range where coupled geostrophic-ageostrophic effects are expected to dominate over the β -effect. This scale range is consistent with the result of the idealized numerical simulations shown in Zhai et al. (2010), where an eddy of 500 km-diameter was used to illustrate the validity of the approximated η -based version of EPW .

574 In summary, approximation (i) of geostrophy is not valid to infer the unapproximated
575 *EPW* in the Agulhas Current region, because the coupled geostrophic-ageostrophic *EKE*
576 flux overall dominate the *EPW* at the mesoscale range ($105 \text{ km} > L > Rd \sim 30 \text{ km}$). We
577 evaluate in the next section, the use of approximation (i) of geostrophy to infer *AEKE*
578 (Table 2), the nonlinear component of *EKE* flux divergence.

579 6 η -based $AEKE_{(i)}$ and unapproximated $AEKE$

580 We first evaluate the mesoscale EKE sources and sinks represented by the η -based
 581 and the unapproximated $AEKE$. We then characterize the main contributions of the two
 582 $AEKE$ s.



583 Figure 4: η -based $AEKE_{(i)}$ and unapproximated $AEKE$ [W m^{-2}] (Table 2). (a) η -based
 584 $AEKE_{(i)}$ ($A + B + C$) split into the contributions of (b) β -effect (A) and (c) work of EKE
 shear (B). (d) Unapproximated $AEKE$ ($A + B + C$) split into the contributions of (e) EKE
 flux ($A + B$) and (f) topographic-contribution (C). (a,d) Vector fields show (a) geostrophic
 EKE flux ($\frac{\rho_0}{2} \int_{-H}^H \mathbf{u}_{g,n} \phi_n ||\mathbf{u}'_{g,n} \phi_n||^2 dz$, with $n = 0 - 1$) and (b) unapproximated EKE
 flux ($\frac{\rho_0}{2} \int_{-H}^H \mathbf{u}_n \phi_n ||\mathbf{u}'_{g,n} \phi_n||^2 dz$, with $n = 0 - 1$) [W m^{-1}]. Note the different colorbar ranges
 between (b) and the other panels. All terms are smoothed with a 75 km-radius Gaussian
 kernel. (cf. Figure 1 for a detailed caption).

585 6.1 Mesoscale EKE sources and sinks from the η -based $AEKE_{(i)}$ and the 586 unapproximated $AEKE$

587 Figure 4a,d shows the η -based $AEKE_{(i)}$ and unapproximated $AEKE$ in the Agulhas
 588 Current region. In the WB region, $AEKE_{(i)}$ and $AEKE$ are in fairly good agreement. Both
 589 $AEKE$ s show a net EKE source (>0 ; Figure 4a,d). The η -based $AEKE_{(i)}$ accounts for
 590 73% of the cumulative EKE source shown by the unapproximated $AEKE$ (the remaining
 591 27% being accounted for by ageostrophic effects). The locally gained EKE is then exported
 592 out of the WB region, eventually into the South Atlantic Ocean or recirculated in the South
 593 Indian Ocean (vector field in Figure 4a,d). The large similarities between $AEKE_{(i)}$ and
 $AEKE$ indicate that approximation (i) of geostrophy is valid for qualitatively inferring
 $AEKE$.

594 The two $AEKE$ s show patterns and magnitudes consistent with the documented vari-
 595 ability of the Agulhas Current (Lutjeharms, 2006; Tedesco et al., 2022). Along the northern

branch of the WB region ($31^{\circ}\text{E} - 26^{\circ}\text{E}$), where the Agulhas Current is stable, both $AEKEs$ are weak (one order of magnitude smaller than in the rest of the domain; Figure 4a,d). Along the southern branch of the WB region ($26^{\circ}\text{E} - 23^{\circ}\text{E}$), both $AEKEs$ are large and generally positive where the shelf curvature increases and the current is documented to be unstable (Lutjeharms, 2006; Tedesco et al., 2022) (Figure 4a,d). In this area, the $AEKEs$ indicate that the eddy dynamics mainly act to energise the mesoscale reservoir, similar to the unapproximated EPW (Figure 2d). Note that $AEKE_{(i)}$, and $AEKE$ in a lesser extend, locally change sign and becomes negative at the tip of the shelf ($24^{\circ}\text{E} - 23^{\circ}\text{E}$), where the topographic constraint on the current is large. This local magnitude difference between the EKE sinks shown by $AEKE_{(i)}$ and $AEKE$ suggests that ageostrophic effects substantially contribute to the mesoscale eddy dynamics at this location.

607 6.2 Main contributions to the η -based $AEKE_{(i)}$

608 The η -based $AEKE_{(i)}$ ($A + B + C$; Table 2; Figure 4a) consists of a geostrophic
 609 EKE flux contribution ($A + B$; Figures 4b,c) and a topographic contribution acting on the
 610 geostrophic EKE flux (C ; not shown), which are of different importance in the Agulhas
 611 Current region. The geostrophic $A + B$ -contribution accounts for 61% of the net $AEKE_{(i)}$,
 612 while the geostrophic topographic contribution accounts for the remaining 39%. Within
 613 the geostrophic EKE flux ($A + B$), the geostrophic EKE shear work (B) is the main contribu-
 614 tion (Figure 4c). The geostrophic EKE shear work (B ; Figure 4c) has locally similar
 615 patterns and magnitudes than $AEKE_{(i)}$ ($A + B + C$; Figure 4a) in the Agulhas Current re-
 616 gion. The velocity divergence contribution (A) corresponds to a negligible nonlinear β -effect
 617 (Figure 4b). It represents a weak EKE sink in the WB region (<0 ; Figure 4b), similar to
 618 its linear analogue acting on $EPW_{(i)}$ ($A1$; Figure 2c). In a nutshell, the η -based $AEKE_{(i)}$
 619 ($A + B + C$; Table 2) is dominated by geostrophic effects in the form of the EKE shear
 620 work (B).

621 6.3 Main contributions to the unapproximated $AEKE$

622 Similar to the η -based $AEKE_{(i)}$, the unapproximated $AEKE$ ($A + B + C$; Table 2)
 623 consists in an EKE flux contribution ($A + B$) and a topographic contribution (C), which
 624 are of different importance in the Agulhas Current region. In the WB region, $AEKE$
 625 ($A + B + C$; Figure 4d) is overall dominated by the positive EKE flux contribution ($A + B$;
 626 Figure 4e), except at the shelf tip ($24^{\circ}\text{E} - 23^{\circ}\text{E}$) where it is locally dominated by the negative
 627 topographic contribution (C ; Figure 4f).

628 The EKE flux contribution ($A + B$) and the topographic contribution (C) do not
 629 account for geostrophic and ageostrophic effects in the same proportions. Approximation
 630 (i) of geostrophy allows to infer a qualitative estimate of the patterns of the EKE flux
 631 contribution ($A + B$; the leading order contribution of $AEKE = A + B + C$). However,
 632 note that the ageostrophic effects acting on A and B are significant. The geostrophic EKE
 633 flux ($A + B$; Figure 4b,c) underestimates the EKE source shown by the unapproximated
 634 analogue ($A + B$; Figure 4e) (underestimation of 35%).

635 On the other hand, approximation (i) of geostrophy limits the estimation of the patterns
 636 and magnitude of the topographic contribution (C ; a secondary contribution to $AEKE =$
 637 $A + B + C$). Geostrophic and unapproximated C -contributions have cumulative values of
 638 opposite sign in the WB region (geostrophic C : 0.65 GW, not shown and unapproximated
 639 C : -0.38 GW in Figure 4f). This indicates that the topographic contribution (C) acting on
 640 $AEKE$ is largely influenced by ageostrophic effects.

641 Note that the EKE source shown by the unapproximated $AEKE$ (2.29 GW; Figure
 642 4d) is due to the accumulation of the barotropic $AEKE$ (0.79 GW; not shown) and 1st
 643 baroclinic $AEKE$ (1.50 GW; not shown). This suggests that the mesoscale $AEKE$ could
 644 be approximated from the contribution of the 1st baroclinic mode. Similar contributions

645 of the barotropic and 1st baroclinic modes are found for the η -based $AEKE_{(i)}$ (mesoscale
646 $AEKE_{(i)}$: 1.67 GW in Figure 4a and barotropic $AEKE_{(i)}$: 0.57 GW and 1st baroclinic
647 $AEKE_{(i)}$: 1.10 GW; not shown).

648 In summary, the η -based $AEKE_{(i)}$ and the unapproximated $AEKE$ support similar
649 paradigms in the Agulhas Current region, because geostrophic effects are a major contributor
650 to $AEKE$ (via the EKE shear work B). However, the accurate estimation of its magnitude
651 using η is less reliable. Indeed, ageostrophic effects also make a significant contribution to
652 $AEKE$ ($A + B + C$), via all its sub-contributions (A , B and C).

653 7 Summary and Discussion

654 In this study, we have investigated the main contributions to the mesoscale *EKE* flux
 655 divergence in the Agulhas Current region. Motivated by opposing η -based and model-
 656 based paradigms of mesoscale eddy dynamics, we aimed to evaluate the validity of the
 657 approximation (i) of geostrophy to infer the mesoscale *EKE* flux divergence in this region.
 658 Geostrophy is a good approximation for inferring mesoscale eddy velocities, but it is a
 659 different matter to use it to infer the *EKE* flux divergence (a tendency term of the *EKE*
 660 budget representing net *EKE* sources and sinks for ocean dynamics in equilibrium; Harrison
 661 & Robinson, 1978). Our analysis used a regional numerical simulation to evaluate the main
 662 contributions of the components of the *EKE* flux divergence, consisting of the eddy pressure
 663 work (*EPW*) and the advection of *EKE* (*AEKE*). In this section, we summarise our main
 664 findings and discuss their implications for the understanding of mesoscale eddy dynamics.

665 7.1 On the use of sea surface height (η) to infer the mesoscale *EKE* flux 666 divergence

667 7.1.1 Eddy pressure work (*EPW*)

668 Based on an approximate calculation of *EPW* using sea surface height (η), Zhai et al.
 669 (2010) showed that western boundaries are mesoscale *EKE* sinks. The η -based diagnosis
 670 of *EPW* is by definition geostrophic. It reduces to the contribution of long baroclinic
 671 Rossby waves (linear β -contribution acting on the 1st baroclinic mode) with additional
 672 approximations to (ii) the vertical structures of mesoscale eddies and (iii) the contribution
 673 of topography. Our results show that none of the approximations (i), (ii) and (iii) are valid
 674 to infer the mesoscale *EPW* in the Agulhas Current region.

675 We first showed that the η -based *EPW*_(i) (considering only approximation (i); Table
 676 1) is dominated by a topographic contribution acting on the barotropic and 1st baroclinic
 677 modes (Figure 2a-d). While the Rossby waves contribution is negligible (A1; Figure 2c).
 678 This invalidates the use of approximations (ii) and (iii). We then showed that the unap-
 679 proximated *EPW* (Table 1) is dominated overall by the coupled geostrophic-ageostrophic
 680 *EKE* flux and locally by topographic interactions (Figures 2d-f,3b). A scale analysis em-
 681 phasised that the coupled geostrophic-ageostrophic *EKE* flux dominates *EPW* at mesoscale
 682 ($L > O(30)$ km), while the β -effect could potentially dominate *EPW* at larger scales
 683 ($L > O(105\text{--}256)$ km).

684 The dominance of ageostrophic effects explains the opposite paradigms supported by
 685 the η -based *EPW*_(i) and the unapproximated *EPW* in the Agulhas Current region. This
 686 also invalidates the use of approximation (i) of geostrophy to infer the mesoscale *EPW* in
 687 this region.

688 7.1.2 Advection of eddy kinetic energy (*AEKE*)

689 We have defined and performed an unapproximated η -based version of the *AEKE*
 690 component (*AEKE*_(i); Table 2) in the Agulhas Current region. Our results show that
 691 approximation (i) of geostrophy is valid to infer a qualitative mesoscale *AEKE*. Unapprox-
 692 imated *AEKE* and η -based *AEKE*_(i) support similar paradigms in the Agulhas Current
 693 region (Figure 4a,d), because geostrophic effects largely contribute to *AEKE* ($A + B + C$;
 694 Figure 4a), via the term of the *EKE* shear work (B ; Figure 4c).

695 Our results support the use of η to qualitatively infer the mesoscale *EKE* source rep-
 696 resented by the *AEKE* component in the western boundary region of the Agulhas Current.
 697 This is furtherly supported by the η -based *AEKE*_(i) performed using observations (Figure
 698 5). The observed η -based *AEKE*_(i) (Table 2) is calculated by combining: (1) η measured
 699 by satellite altimetry, (2) vertical modes calculated from time-averaged stratification de-
 700 rived from the WOCE climatology, and (3) $\lambda_n = \frac{\eta_n}{\eta}$ (Eq. 2.3.1) and $\alpha_n = \frac{\eta'_n}{\eta'}$ (Eq. 2.3.1)

parameters — modulating η according to vertical modes — derived from our numerical simulation at each time step and spatially averaged over the WB region. The observed η -based $AEKE_{(i)}$ shows a mesoscale EKE source in the WB region in fairly good agreement with the modeled η -based $AEKE_{(i)}$ and the modeled unapproximated $AEKE$ (Figures 5a and 4a,d). It shows a large EKE source extending from about 26°E to the Retroflection (20°E), whose cumulative value is 43% and 32% of that of the modeled η -based $AEKE_{(i)}$ and the unapproximated $AEKE$, respectively.

Note that the fairly good qualitative agreement between observed η -based $AEKE$ and modeled versions of $AEKE$ (Figures 5a and 4a,d) highlights a reliable alternative to approximation (ii). The contribution of the barotropic and 1st baroclinic modes to η , and hence to $AEKE$, can be reliably approximated in small regions using spatially averaged model-based partitioning of the modal η .

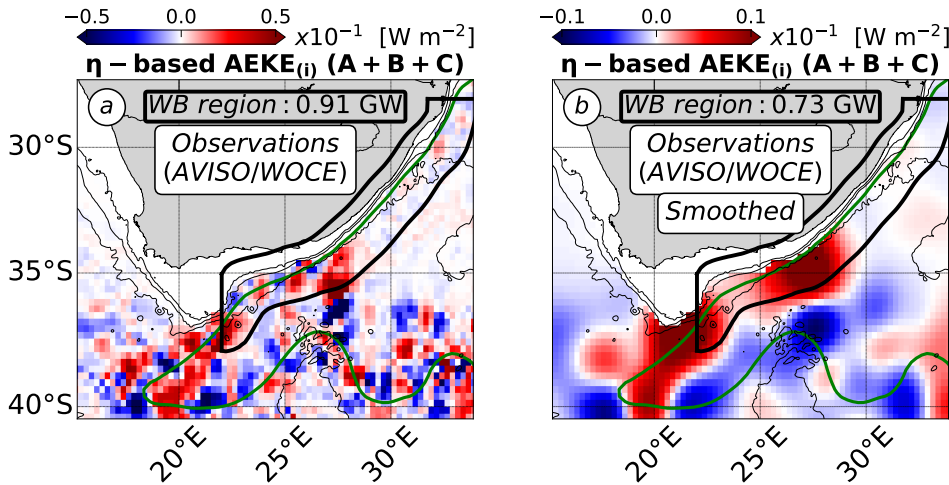


Figure 5: Observed η -based $AEKE_{(i)}$ [W m^{-2}] (Table 2). (a) Unsmoothed and (b) smoothed version of the observed η -based $AEKE_{(i)}$ performed using a combination of satellite altimetry data (AVISO), climatological data (WOCE) and model-based parameter (Eq. 7, 8). For (b), the smoothing radius is 75 km as for Figures 2, 4. Note the different colorbar range between the two panels. (cf. Figure 1 for a detailed caption).

7.1.3 Conclusion on the mesoscale EKE flux divergence (EPW and AEKE)

Our thorough analysis of the contributions to EPW and $AEKE$ (forming the EKE flux divergence) allows us to conclude on the use of η to infer mesoscale EKE sources and sinks in the Agulhas Current region. $AEKE$ represents the larger cumulative contribution ($AEKE$: 2.29 GW) to the EKE flux divergence in the WB region ($EPW + AEKE$: 3.12 GW; Figures 2d, 4d). Although, the approximation of geostrophy (i) does not allow to infer EPW (Figures 2a,d), it does allow to infer a qualitative estimate of $AEKE$ (73%; Figure 4a,d). This indicates that a qualitative estimate of the EKE flux divergence can be inferred from η , via the $AEKE$ component. In the model, using the η -based $AEKE_{(i)}$ as a proxy for the EKE flux divergence would lead to an underestimation of 46% of the EKE source in the WB region of the Agulhas Current (Figure 4a,d). From observations, however, the underestimation appears to be significantly larger (76%; Figure 5b and 4d).

725 Further investigation would therefore be required to conclude on the use of η measured by
 726 satellite altimetry to reliably infer the magnitude of the *EKE* source in this region.

727 Our results support the use of η to infer a qualitative estimate of the mesoscale *AEKE*,
 728 and subsequently of the mesoscale *EKE* flux divergence, but for fundamentally different
 729 reasons than Zhai et al. (2010). Zhai et al. (2010) used approximation (i) of geostrophy
 730 based on the hypothesis that long baroclinic Rossby waves are the main contributor to the
 731 *EKE* flux divergence. We show in this study that geostrophic effects make a significant
 732 contribution to the *EKE* flux divergence in the Agulhas Current region, via the advection
 733 of geostrophic *EKE* by geostrophic mean and eddy flows (*AEKE*).

734 7.2 On the mesoscale eddy energy budget at western boundaries

735 7.2.1 Main contributions acting on the mesoscale *EKE* flux divergence

736 The paradigm of a mesoscale eddies graveyard at western boundaries supported by
 737 Zhai et al. (2010) relies on long baroclinic Rossby waves (β -effect) as the main contributor
 738 to the mesoscale *EKE* flux divergence. Our results suggest that the mesoscale *EKE* flux
 739 divergence may not be dominated by the β -effect in western boundary regions.

740 Our scaling analysis showed that the magnitude of the linear β -contribution to *EPW*
 741 depends on metrics that provide a measure of dynamical and regional characteristics (Ro :
 742 mesoscale eddy Rossby number and the β parameter, respectively). The β parameter is
 743 usually low compared to Ro at mid-latitudes, resulting in a weak β -contribution to *EPW*.
 744 However, the β parameter is larger at low latitudes, suggesting that these regions may be
 745 more conducive to a large linear β -contribution to the *EKE* flux divergence. However, topographic
 746 interactions are large at western boundaries regardless of latitude. The topographic
 747 contribution may therefore be as large or larger than the β -effect contribution to the *EKE*
 748 flux divergence at western boundaries of all latitudes.

749 7.2.2 Main sources and sinks of *EKE*

750 The positive *EKE* flux divergence indicates that the mesoscale eddy dynamics in
 751 the WB region of the Agulhas Current are locally dominated by processes energising the
 752 mesoscale *EKE* reservoir. A recent study characterized the processes contributing to the
 753 mesoscale *EKE* source in this region (Tedesco et al., 2022). They showed that the local
 754 generation of mesoscale eddies — due to barotropic and mixed barotropic-baroclinic instabilities
 755 of the Agulhas Current — overcomes the local decay of locally- and remotely generated
 756 mesoscale eddies — mainly due to bottom stress and topographically channeled processes
 757 —. Our current study complements the process study of Tedesco et al. (2022), by showing
 758 (1) that the local mesoscale *EKE* source is largely redistributed in space by the advection
 759 done by geostrophic mean and eddy flows and (2) that this net spatial redistribution can
 760 be qualitatively inferred from η fields.

761 We suggest that the *EKE* flux divergence at western boundaries may vary with the
 762 presence or absence of a western boundary current. However, additional studies of other
 763 western boundary regions — with or without a western boundary current and for a broad
 764 latitudinal range — would be required to draw conclusions about the mesoscale eddy dy-
 765 namics at each western boundary. The mesoscale *EKE* flux divergence could represent an
 766 *EKE* sink in the western boundary regions without a western boundary current, as topo-
 767 graphically channeled processes damping mesoscale eddies would locally dominate. This is
 768 supported by studies based on *in situ* observations and idealized numerical simulations, for
 769 western boundary regions without a western boundary current (Evans et al., 2020; Z. Yang
 770 et al., 2021; Evans et al., 2022). The mesoscale *EKE* flux divergence could represent an
 771 *EKE* source in western boundary regions with a western boundary current, as the local
 772 generation of mesoscale eddies would dominate the damping effect of topographic interac-
 773 tions, similar to the Agulhas Current region (Tedesco et al., 2022). This is supported by the

intense generation of mesoscale eddies by flow instabilities documented in several western boundary currents (Halo et al., 2014; Kang & Curchitser, 2015; Gula et al., 2015; Y. Yang & Liang, 2016; Yan et al., 2019; Li et al., 2021; Jamet et al., 2021; Tedesco et al., 2022). Furthermore, an exhaustive description of the processes contributing to mesoscale eddy decay in western boundary regions including a western boundary current, should include eddy-mean interactions in addition to topographic interactions (Holloway, 1987; Adcock & Marshall, 2000; Chen et al., 2014; Tedesco et al., 2022).

781 **Appendix A Observed and modeled sea surface height (η) variance in
782 the Agulhas Current region**

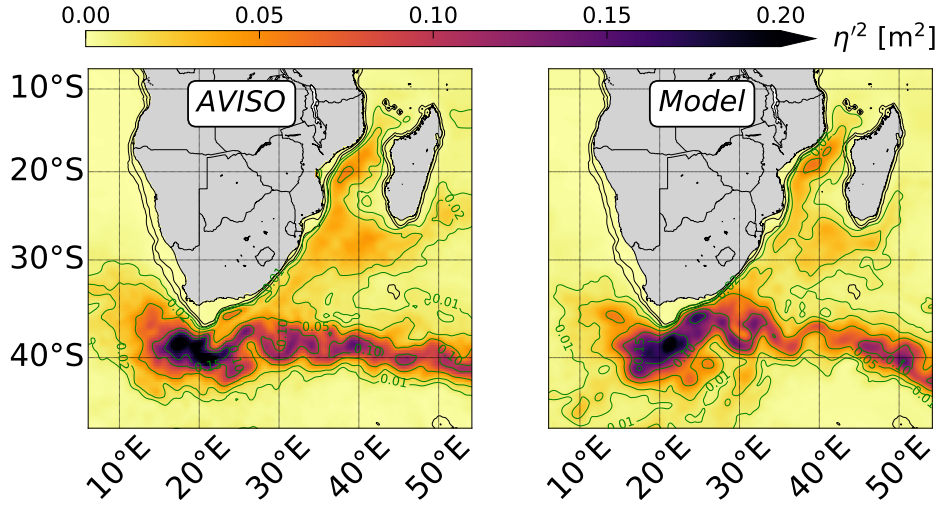


Figure A1: Observed and modeled mesoscale variability at the surface in the Agulhas Current system. η variance (η'^2) [m^2] performed from (a) a numerical simulation ($\text{dx} \sim 7.5 \text{ km}$) and (b) satellite altimetry data (AVISO). Green contours denote isolines of η variance and black contours denote 300 m and 1000 m isobaths.

The evaluation of the η -based version of the EKE flux divergence defined by Zhai et al. (2010) ($EPW_{(i,ii,iii)}$) in the model and observations, suggest that the modeled mesoscale eddy field might be weaker compared to observations (*cf.* section 3.3). The model of horizontal resolution of $\text{dx} \sim 2.5 \text{ km}$, used in this study, is forced at the boundaries at each time step by a parent model of $\text{dx} \sim 7.5 \text{ km}$. The parent simulation resolve mesoscale eddies of scales 50 km–100 km, but may underestimate their magnitude due to a too weak inverse turbulent cascade at smaller scales. This process has been shown to be of importance in the Subgyre regions of the Agulhas Current system (Schubert et al., 2020).

Based on this assumption, we evaluate the modeled mesoscale variability (η variance) simulated by the parent simulation ($\text{dx} \sim 7.5 \text{ km}$) against satellite altimetry data (Figure A1). The parent simulation covers the western part of the subtropical gyre of the Indian Ocean. The Agulhas Current originates from the lower end of the Mozambique Channel (32.5°E), where it feeds upon the Mozambique Current and the East Madagascar Current. The Agulhas Current flows along the South African coastline to the South African tip (20°E). From there, it Retroflects and become the Agulhas Return Current flowing eastward into the South Indian Ocean.

Modeled η variance represents the variability of the Agulhas Current system in overall good agreement with observations. The Mozambique Current, the East Madagascar Current and the Agulhas Current show moderate value of η variance ($O(0.02\text{--}0.03) \text{ m}^2$). The Agulhas Retroflection and the Agulhas Return Current show the largest η variance ($O(0.05\text{--}0.15) \text{ m}^2$). In the context of our study, a relevant difference is the weaker modeled η variance in the Subgyre region ($35^\circ\text{E} - 45^\circ\text{E}$ and $25^\circ\text{S} - 35^\circ\text{S}$). There, the model shows moderate value of smaller extend than in observations. This confirms that the modeled mesoscale

806 eddies propagating westward through the Subgyre toward the Agulhas Current region have
807 a weaker amplitude than in observations. This supports the weaker amplitude of the *EKE*
808 sink in the WB region shown by the modeled $EPW_{(i,ii,iii)}$ compared to observed one, to be
809 due to a weaker modeled mesoscale eddy field forced at the boundaries.

810 **Appendix B Sensitivity of the unapproximated EPW to spatial smoothing**
 811

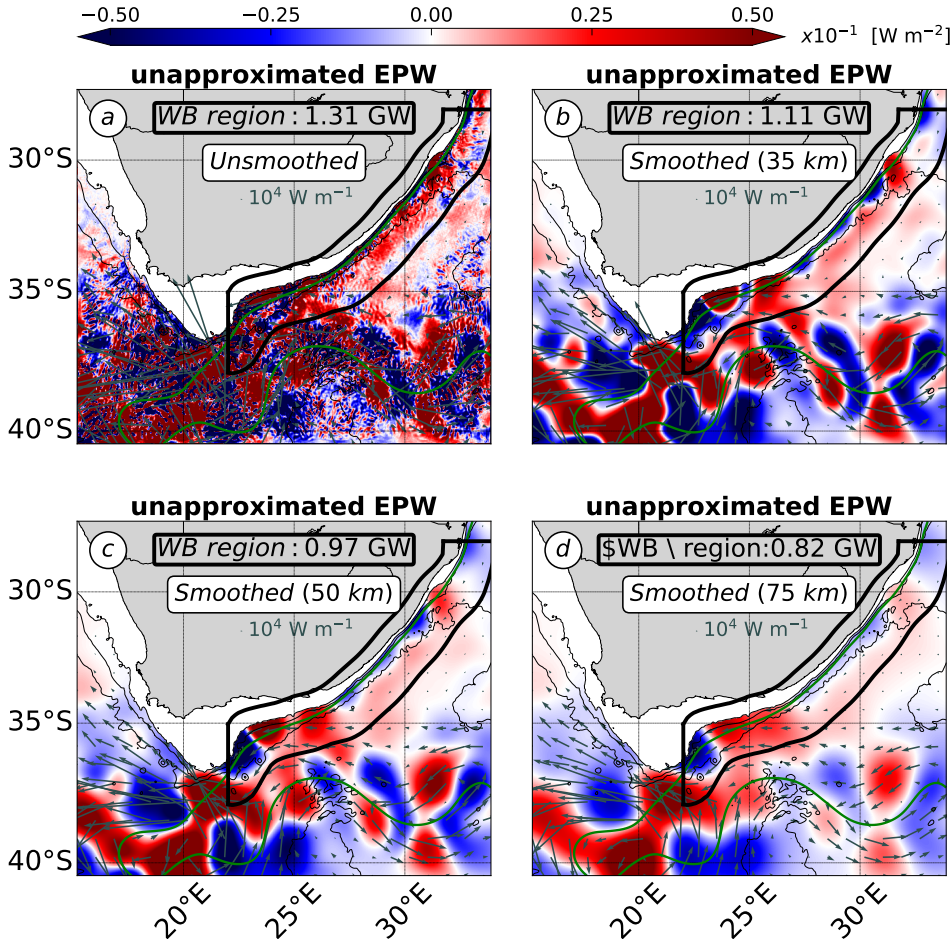


Figure B1: Sensitivity of the unapproximated EPW [W m^{-2}] (Table 1) to spatial smoothing. EPW shown for (a) no spatial smoothing and (b,c,d) spatial smoothing of different radius from (b) 35 km, (c) 50 km to (d) 75 km. Vector fields show the corresponding smoothed EKE flux ($\int_{-H}^{\eta} \mathbf{u}'_n p'_n \phi_n^2 dz$, with $n = 0 - 1$) [W m^{-1}]. (cf. Figure 1 for a detailed caption).

The unapproximated EPW (Table 1) is spatially smoothed to emphasise the large-scale patterns driving its cumulative contribution in the WB region (Figure B1). The unsmoothed EPW is characterized by small-scales patterns that are the most intense at topographic features — shelf slope (1000 m isobath), seamounts, canyons, roughness, among others — locally peaking at $O(2.5 - 10)$ W m^{-2} (Figure B1a). In the WB region, the intense small-scales patterns of the unapproximated EPW are larger by one or two order of magnitude than the unsmoothed $EPW_{(i,ii,iii)}$ ($O(0.01)$ W m^{-2} ; Figure 2a). However, the magnitude of the cumulative contribution of EPW (1.31 GW; Figure B1a) is close to the one of $EPW_{(i,ii,iii)}$ (-1.32 GW; Figure 1b) in this region, regardless of the intense small-scale patterns. It indicates that the intense small-scale patterns locally compensate and do not

822 significantly contribute to the cumulative *EPW* in the WB region.

823
824 The sensitivity of the unapproximated *EPW* to the smoothing is shown using a Gaussian
825 kernel of progressively increasing length scale: from 35 km (the spatially-averaged
826 Rossby deformation radius in region the modeled region) to 50 km and 75 km (two typical
827 mesoscale eddies radii at mid-latitudes; Chelton et al., 2011). The patterns of *EPW* change
828 with the different smoothing length scales, but the order of magnitude of the cumulative
829 contribution in the WB region is reasonably unchanged ($\leq 30\%$; Figure B1). A similar
830 sensitivity to the smoothing is found for the unapproximated *AEKE* ($\leq 20\%$; not shown).

831

832 In the study, the label 'smoothed' in Figures refers to the Gaussian kernel using a
833 75 km-radius. The smoothings using 50 km- and 75 km-radius result in fairly close cu-
834 mulative *EPW* in the WB region (Figures B1c,d). However, the 75 km-radius smoothing
835 provides smoother patterns, emphasizing the most the large-scale patterns driving the *EPW*
836 cumulative in the WB region, and facilitating the most its comparison with $EPW_{(i,ii,iii)}$
837 (Table 1; Figures 1b).

838 Appendix C Partitioning of sea surface height (η) variance into the barotropic 839 and 9 first baroclinic vertical modes

840 In order to assess the validity of approximations (ii) and (iii) to infer EPW , we pro-
841 gressively relax the use of the approximations when inferring the η -based EPW term (*cf.*
842 section 4). Relaxing the use of approximation (ii) of η primarily reflecting the 1st baroclinic
843 mode, requires to evaluate the partitioning of the η variance into the different vertical modes
844 ($\alpha_n^2 = \frac{\eta_n'^2}{\eta'^2}$; Eq. 8 in section 2.3.1). η is a 2-dimensional field and cannot be straightforwardly
845 projected onto the vertical mode base. However, the modal coefficient for η (η_n') can be
846 inferred such as: $\eta_n' = \frac{p_n'(z=0)}{\rho_0 g}$, using the modal pressure at $z = 0$ m and the hydrostatic
847 relationship.

The modal expression of the η variance (η'^2) and α_n^2 are defined as follows:

$$\begin{aligned} \eta'^2 &= \sum_{n=0}^{\infty} \eta_n' \sum_{m=0}^{\infty} \eta_m' \\ \eta'^2 &= \sum_{n=0}^{\infty} \eta_n'^2 + \underbrace{\sum_{n=0}^{\infty} \sum_{m \neq n}^{\infty} \eta_n' \eta_m'}_{\text{Intermodal coupling } (C_{nm})} \\ \eta'^2 &= \sum_{n=0}^{\infty} \eta_n'^2 + C_{nm} \end{aligned} \quad (\text{C1})$$

$$\alpha_n^2 = \frac{\eta_n'^2}{\eta'^2} \text{ and } \alpha_{nm} = \frac{C_{nm}}{\eta'^2} \quad (\text{C2})$$

848 The modal expression of the variance of η (Eq. C1) involves an intermodal coupling
849 term(C_{nm}). It corresponds to a phase-locked combination of vertical modes at the
850 surface due to the modal correlation in time (Wunsch, 1997; Scott & Furnival, 2012). The
851 degree of the surface modal correlation ($\frac{\sum_{n=0}^9 \eta_n'^2}{\sum_{n=0}^9 \eta_n'^2 + C_{nm}}$) is 1.8 in average in our numerical
852 simulation, which is consistent with the 2-3 factor determined at global-scale from *in situ*
853 data (Wunsch, 1997). However, it must be noted that the unapproximated EPW (Table
854 1) only accounts for the contribution of individual modes ($n = 0$ and $n = 1$). The coupling
855 term C_{nm} is of importance for accurately decomposing η into vertical modes, but it does not
856 contribute to the vertically-integrated form of the mesoscale EKE flux divergence consid-
857 ered in this study. Indeed, EPW involves the orthogonality condition resulting in canceling
858 out the contribution of C_{nm} to EPW .

859 Using our numerical simulation of the Agulhas Current, we inferred α_n^2 the partitioning
860 of the η variance into the barotropic and 9 first baroclinic modes (Figure C1). The barotropic
861 and 10 first baroclinic modes account for 85-100% of the modeled η variance in the region
862 (not shown).

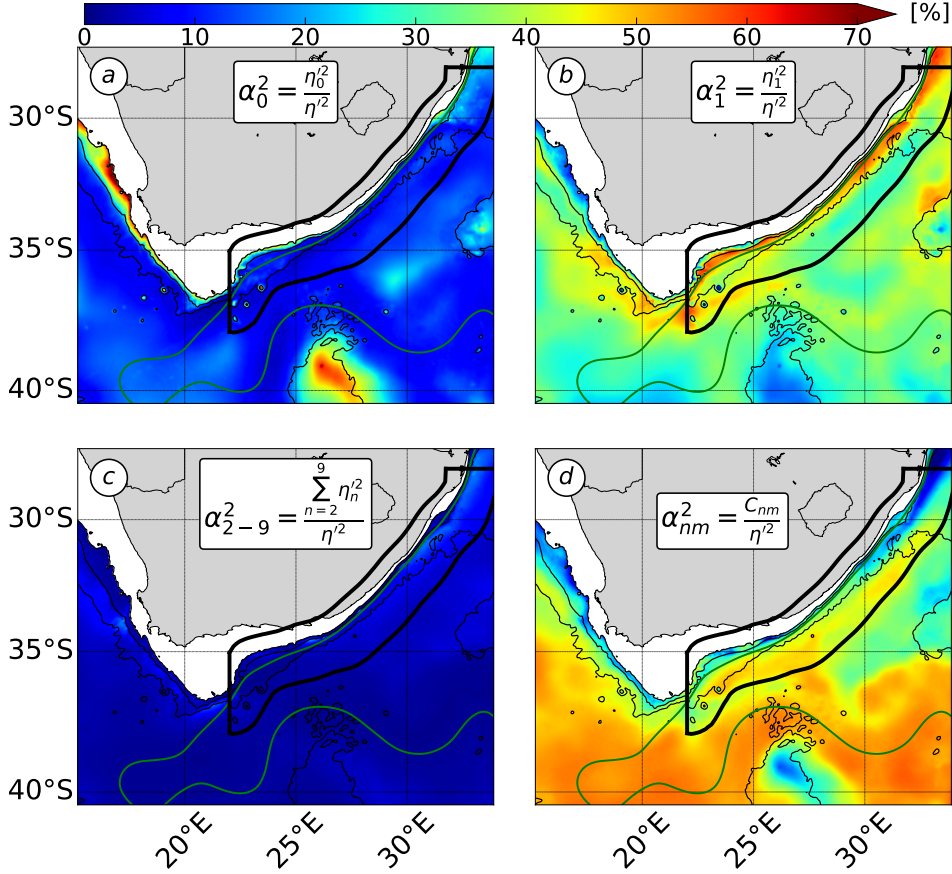


Figure C1: Partitioning of the sea surface height variance into categories of vertical modes ($\alpha_n^2 = \frac{\eta_n'^2}{\eta'^2}$) [%], including (a) the barotropic mode ($n = 0$), (b) the 1st baroclinic mode ($n = 1$), (c) higher baroclinic modes ($n = 2 - 9$) and (d) the intermodal coupling at the surface (C_{nm}). (cf. Figure 1 for a detailed caption).

In the WB region, The η variance mainly partitions into the 1st baroclinic mode ($38 \pm 2\%$; Figure C1b) and C_{nm} the intermodal coupling term ($36 \pm 2\%$; Figure C1d). It partitions more weakly, but still significantly into the barotropic mode ($16 \pm 4\%$) (Figure C1a). This is partially consistent with the usual interpretation of η primarily reflecting the 1st baroclinic mode (Wunsch, 1997; Smith & Vallis, 2001). However, it also indicates that the vertical structure of mesoscale eddies — formally represented by the combination of the barotropic ($n = 0$) and 1st baroclinic modes ($n = 1$) (Wunsch, 2007; Smith & Vallis, 2001; Venaille et al., 2011; Tedesco et al., 2022) — can be accurately inferred from η field. This enables us to relax approximation (ii) and compute the unapproximated η -based $EPW_{(i)}$ (defined as the sum of the barotropic and 1st baroclinic contributions) from the modeled η field (cf. section 4).

874 **Appendix D Alternative definition of the cross-over scale based on the**
 875 **Rhines scale**

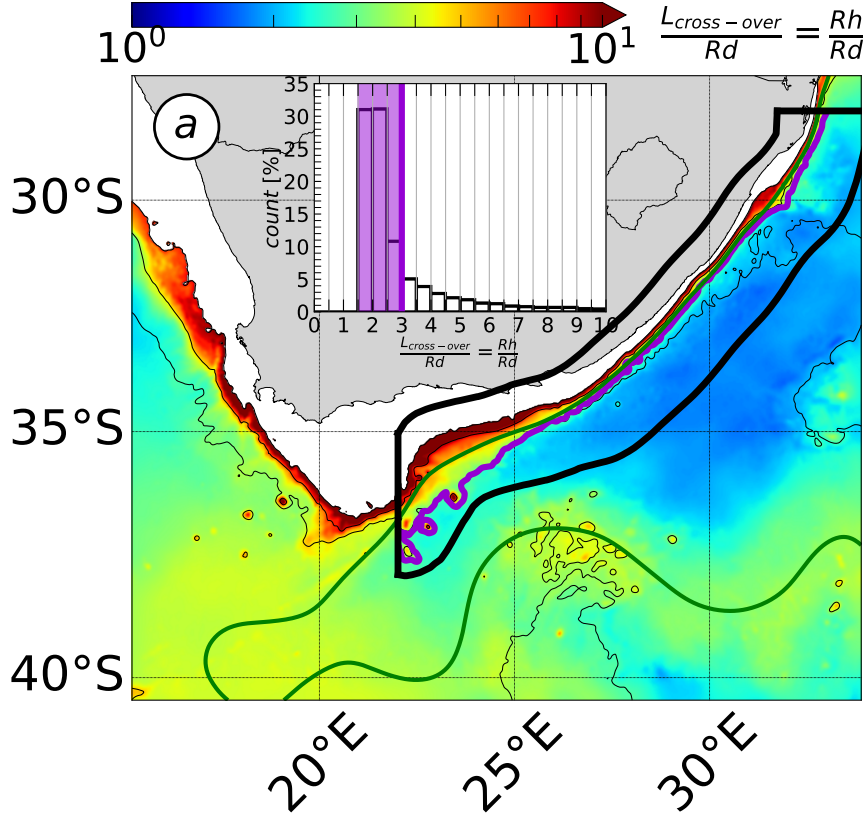


Figure D1: Alternative cross-over scale ($L_{g,ag} = Rh = \frac{1}{H} \int_{-H}^{\eta} \left(\sqrt{\frac{\|\mathbf{u}'\|}{\beta}} \right) dz$, with $\|\mathbf{u}'\|$ the magnitude of mesoscale eddies velocity) in the Agulhas Current region. (a) Ratio between the alternative cross-over scale and the characteristic length scale of mesoscale eddies (Rossby deformation radius; Rd). In the barplot, counts of (a) in the WB region are in [%] and shaded area shows the 70 % percentile. In the map, purple contours show 70 % percentile of (a) in the physical space. (cf. Figure 1 for a detailed caption)

876 Our scale analysis allows us to define a cross-over scale, marking the transition between
 877 regimes of large ageostrophic effects and large β -effect acting on the unapproximated EPW
 878 (cf. section 5.2.2). Using quasi-geostrophic scalings for horizontal velocity and pressure,
 879 the cross-over scale is determined by the magnitude of the mesoscale eddies Rossby number
 880 (Ro) with respect to the β -parameter (Eq. 15). The definition of the cross-over scale is
 881 not unique and changes with the scaling of Ro . Using $Ro = \frac{U'}{fL}$ (instead of $Ro = \zeta'_{RMS} f$
 882 in section 5.2.2), we define an alternative cross-over scale, which corresponds to the Rhines
 883 scale ($Rh = \frac{1}{H} \int_{-H}^{\eta} \left(\sqrt{\frac{\|\mathbf{u}'\|}{\beta}} \right) dz$, with $\|\mathbf{u}'\|$ the magnitude of mesoscale eddies velocity).

In the quasi-geostrophic theory, the Rhines scale marks the transition from an advectively-dominated (nonlinear) dynamical regime ($Rh \gg L$; with L the characteristic length scale of eddies) to a Rossby waves-dominated (linear) dynamical regime ($Rh \ll L$) (Rhines, 1975). This definition of the cross-over scale shows that evaluating the dominant regime of the mesoscale *EPW* is therefore similar to evaluating the mesoscale eddies dynamical regime.

In the Agulhas Current region, the typical values of the Rhines scale support the conclusions arising from the version of the cross-over scale presented in the study (Eq. 15 and Figure 3b). The Rhines scale indicates that mesoscale eddies fall in the range of large coupled geostrophic-ageostrophic *EPW* with respect to the linear β -contribution (Rh in $O(1.5\text{--}3)Rd$ in 70% of the WB region and larger values at the inner front; Figure D1). This results shows that in the WB region of the Agulhas Current, mesoscale eddies fall in the range of large coupled geostrophic-ageostrophic flux — with respect to linear β -effect — as a result of mesoscale eddies being characterized by a nonlinear dynamical regime ($Rh \gg Rd$) — and not a linear wave dynamical regime ($Rh \ll L$) —. Nonlinear dynamics of mesoscale eddies has been characterized from satellite altimetry data, as documented by Chelton et al. (2011).

901 Open Research Section

902 WOES36 model outputs are available online at [http://dap.saeon.ac.za/thredds/
903 catalog/SAEON.EGAGASINI/2019.Penven/DAILY_MEANS/1_36_degree/catalog.html](http://dap.saeon.ac.za/thredds/catalog/SAEON.EGAGASINI/2019.Penven/DAILY_MEANS/1_36_degree/catalog.html) The AVISO
904 data are available at www.aviso.altimetry.fr, the WOA18 and WOCE climatologies are
905 available at www.nodc.noaa.gov/OC5/woa18/ and [https://icdc.cen.uni-hamburg.de/
906 thredds/catalog/ftpthredds/woce/catalog.htm](https://icdc.cen.uni-hamburg.de/thredds/catalog/ftpthredds/woce/catalog.htm).

907 Acknowledgments

908 This work was granted access to the HPC resources of IDRIS under the allocation A0040107630
909 made by GENCI at Paris, France, and of the HPC facilities DATARMOR of “Pôle de Calcul
910 Intensif pour la Mer” at Ifremer, Brest, France. This work was supported by the Ifremer
911 and the Brittany region for PhD funding. We also gratefully acknowledge support from
912 the French National Agency for Research (ANR) through the projects DEEPER (ANR-19-
913 CE01-0002-01) and the project DIEGO of the CNES/TOSCA SWOT program.

914 **References**

- 915 Adcock, S., & Marshall, D. (2000). Interactions between geostrophic eddies and the mean
 916 circulation over large-scale bottom topography. *Journal of physical oceanography*, 30(12),
 917 3223–3238.
- 918 Capó, E., Orfila, A., Mason, E., & Ruiz, S. (2019). Energy conversion routes in the western
 919 mediterranean sea estimated from eddy–mean flow interactions. *Journal of Physical
 920 Oceanography*, 49(1), 247–267.
- 921 Chelton, D., Deszoeke, R., Schlax, M., El Naggar, K., & Siwertz, N. (1998). Geographical
 922 variability of the first baroclinic Rossby radius of deformation. *Journal of Physical
 923 Oceanography*, 28(3), 433–460.
- 924 Chelton, D., Schlax, M., & Samelson, R. (2011). Global observations of nonlinear mesoscale
 925 eddies. *Progress in oceanography*, 91(2), 167–216.
- 926 Chelton, D., Schlax, M., Samelson, R., & de Szoeke, R. (2007). Global observations of large
 927 oceanic eddies. *Geophysical Research Letters*, 34(15).
- 928 Chen, R., Flierl, G., & Wunsch, C. (2014). A description of local and nonlocal eddy–
 929 mean flow interaction in a global eddy-permitting state estimate. *Journal of Physical
 930 Oceanography*, 44(9), 2336–2352.
- 931 Cushman-Roisin, B., & Beckers, J.-M. (2011). *Introduction to geophysical fluid dynamics:
 932 physical and numerical aspects*. Academic press.
- 933 Debreu, L., Marchesiello, P., Penven, P., & Chambon, G. (2012). Two-way nesting in split-
 934 explicit ocean models: Algorithms, implementation and validation. *Ocean Modelling*,
 935 49–50, 1–21.
- 936 Ducet, N., Traon, P.-Y. L., & Reverdin, G. (2000). Global high-resolution mapping of ocean
 937 circulation from TOPEX/Poseidon and ERS-1 and-2. *Journal of Geophysical Research:
 938 Oceans*, 105(C8), 19477–19498.
- 939 Eliot, S., & Beal, L. M. (2015). Characteristics, Energetics, and Origins of Agulhas
 940 Current Meanders and Their Limited Influence on Ring Shedding. *Journal of Physical
 941 Oceanography*, 45(9), 2294–2314. doi: 10.1175/JPO-D-14-0254.1
- 942 Evans, D., Frajka-Williams, E., & Garabato, A. N. (2022). Dissipation of mesoscale eddies
 943 at a western boundary via a direct energy cascade. *Scientific Reports*, 12(1), 1–13.
- 944 Evans, D., Frajka-Williams, E., Garabato, A. N., Polzin, K., & Forryan, A. (2020).
 945 Mesoscale eddy dissipation by a ‘zoo’ of submesoscale processes at a western boundary.
 946 *Journal of Geophysical Research: Oceans*, e2020JC016246.
- 947 Ferrari, R., & Wunsch, C. (2009). Ocean circulation kinetic energy: Reservoirs, sources,
 948 and sinks. *Annual Review of Fluid Mechanics*, 41.
- 949 Gill, A. (1982). *Atmosphere-ocean dynamics (international geophysics series)*. academic
 950 press.
- 951 Gill, A., Green, J., & Simmons, A. (1974). Energy partition in the large-scale ocean
 952 circulation and the production of mid-ocean eddies. *Deep sea research and oceanographic
 953 abstracts*, 21(7), 499–528.
- 954 Gouretski, V., & Koltermann, K. (2004). WOCE global hydrographic climatology. *Berichte
 955 des BSH*, 35, 1–52.
- 956 Gula, J., Molemaker, M., & McWilliams, J. (2015). Gulf Stream dynamics along the
 957 Southeastern U.S. Seaboard. *J. Phys. Oceanogr.*, 45(3), 690–715.
- 958 Halo, I., Penven, P., Backeberg, B., Ansorge, I., Shillington, F., & Roman, R. (2014).
 959 Mesoscale eddy variability in the southern extension of the East Madagascar Current:
 960 Seasonal cycle, energy conversion terms, and eddy mean properties. *Journal of Geophys-
 961 ical Research: Oceans*, 119(10), 7324–7356.
- 962 Harrison, D. E., & Robinson, A. R. (1978). Energy analysis of open regions of turbulent
 963 flows—Mean eddy energetics of a numerical ocean circulation experiment. *Dynamics of
 964 Atmospheres and Oceans*, 2(2), 185–211.
- 965 Holloway, G. (1987). Systematic forcing of large-scale geophysical flows by eddy-topography
 966 interaction. *Journal of Fluid Mechanics*, 184, 463–476.

- 967 Jamet, Q., Deremble, B., Wienders, N., Uchida, T., & Dewar, W. (2021). On wind-driven
 968 energetics of subtropical gyres. *Journal of Advances in Modeling Earth Systems*, 13(4),
 969 e2020MS002329.
- 970 Kang, D., & Curchitser, E. (2015). Energetics of eddy-mean flow interactions in the Gulf
 971 Stream region. *Journal of Physical Oceanography*, 45(4), 1103–1120.
- 972 Kelly, S. (2016). The vertical mode decomposition of surface and internal tides in the
 973 presence of a free surface and arbitrary topography. *Journal of Physical Oceanography*,
 974 46(12), 3777–3788.
- 975 Kelly, S., Nash, J., & Kunze, E. (2010). Internal-tide energy over topography. *Journal of
 976 Geophysical Research: Oceans*, 115(C6).
- 977 Kelly, S., Nash, J., Martini, K., Alford, H. M., & Kunze, E. (2012). The cascade of tidal
 978 energy from low to high modes on a continental slope. *Journal of physical oceanography*,
 979 42(7), 1217–1232.
- 980 Li, J., Roughan, M., & Kerry, C. (2021). Dynamics of interannual eddy kinetic energy mod-
 981 ulations in a western boundary current. *Geophysical Research Letters*, e2021GL094115.
- 982 Lutjeharms, J. (2006). *The Agulhas Current* (Vol. 2). Springer.
- 983 Lutjeharms, J., Boebel, O., & Rossby, H. (2003). Agulhas cyclones. *Deep Sea Research
 984 Part II: Topical Studies in Oceanography*, 50(1), 13–34.
- 985 Lutjeharms, J., Penven, P., & Roy, C. (2003). Modelling the shear edge eddies of the
 986 southern agulhas current. *Continental Shelf Research*, 23(11-13), 1099–1115.
- 987 Masuda, A. (1978). Group velocity and energy transport by Rossby waves. *Journal of
 988 Oceanography*, 34(1), 1–7.
- 989 Müller, P., McWilliams, J., & Molemaker, M. (2005). *Routes to dissipation in the ocean:
 990 The 2D/3D turbulence conundrum*. Cambridge University Press Cambridge.
- 991 Nikurashin, M., & Ferrari, R. (2010). Radiation and dissipation of internal waves generated
 992 by geostrophic motions impinging on small-scale topography: Theory. *Journal of Physical
 993 Oceanography*, 40(5), 1055–1074.
- 994 Perfect, B., Kumar, N., & Riley, J. (2020). Energetics of Seamount Wakes. Part I: Energy
 995 Exchange. *Journal of Physical Oceanography*, 50(5), 1365–1382.
- 996 Rhines, P. (1975). Waves and turbulence on a beta-plane. *Journal of Fluid Mechanics*,
 997 69(3), 417–443.
- 998 Schubert, R., Gula, J., & Biastoch, A. (2021). Submesoscale flows impact Agulhas leakage
 999 in ocean simulations. *Communications Earth & Environment*, 2(1), 1–8.
- 1000 Schubert, R., Gula, J., Greatbatch, R., Baschek, B., & Biastoch, A. (2020). The Sub-
 1001 mesoscale Kinetic Energy Cascade: Mesoscale Absorption of submesoscale Mixed Layer
 1002 Eddies and Frontal Downscale Fluxes. *Journal of Physical Oceanography*, 50(9), 2573–
 1003 2589.
- 1004 Scott, R., & Furnival, D. (2012). Assessment of traditional and new eigenfunction bases
 1005 applied to extrapolation of surface geostrophic current time series to below the surface
 1006 in an idealized primitive equation simulation. *Journal of physical oceanography*, 42(1),
 1007 165–178.
- 1008 Shchepetkin, A., & McWilliams, J. (2005). The Regional Oceanic Modeling System
 1009 (ROMS): A split-explicit, free-surface, topography-following- coordinate ocean model.
 1010 *Ocean Modelling*, 9, 347-404.
- 1011 Smith, K., & Vallis, G. (2001). The scales and equilibration of midocean eddies: Freely
 1012 evolving flow. *Journal of Physical Oceanography*, 31(2), 554–571.
- 1013 Soufflet, Y., Marchesiello, P., Lemarié, F., Jouanno, J., Capet, X., Debreu, L., & Benshila,
 1014 R. (2016). On effective resolution in ocean models. *Ocean Modelling*, 98, 36–50.
- 1015 Tedesco, P., Gula, J., Penven, P., & Ménesguen, C. (2022). Mesoscale Eddy Kinetic Energy
 1016 budgets and transfers between vertical modes in the Agulhas Current. *Journal of Physical
 1017 Oceanography*.
- 1018 Venaille, A., Vallis, G., & Smith, K. (2011). Baroclinic turbulence in the ocean: Analysis
 1019 with primitive equation and quasigeostrophic simulations. *Journal of Physical Oceanog-
 1020 raphy*, 41(9), 1605–1623.

- 1021 Wunsch, C. (1997). The vertical partition of oceanic horizontal kinetic energy. *Journal of*
1022 *Physical Oceanography*, 27(8), 1770–1794.
- 1023 Wunsch, C. (2007). The past and future ocean circulation from a contemporary perspective.
1024 *Geophysical Monograph-American Geophysical Union*, 173, 53.
- 1025 Yan, X., Kang, D., Curchitser, E., & Pang, C. (2019). Energetics of eddy–mean flow
1026 interactions along the western boundary currents in the North Pacific. *Journal of Physical*
1027 *Oceanography*, 49(3), 789–810.
- 1028 Yang, Y., & Liang, X. S. (2016). The instabilities and multiscale energetics underlying
1029 the mean–interannual–eddy interactions in the Kuroshio Extension region. *Journal of*
1030 *Physical Oceanography*, 46(5), 1477–1494.
- 1031 Yang, Z., X., Z., Marshall, D., & Wang, G. (2021). An Idealized Model Study of Eddy
1032 Energetics in the Western Boundary “Graveyard”. *Journal of Physical Oceanography*,
1033 51(4), 1265–1282.
- 1034 Yankovsky, E., Zanna, L., & Smith, K. (2022). Influences of Mesoscale Ocean Eddies on
1035 Flow Vertical Structure in a Resolution-Based Model Hierarchy. *Earth and Space Science*
1036 Open Archive, 60. Retrieved from <https://doi.org/10.1002/essoar.10511501.1> doi:
1037 10.1002/essoar.10511501.1
- 1038 Zhai, X., Johnson, H., & Marshall, D. (2010). Significant sink of ocean-eddy energy near
1039 western boundaries. *Nature Geoscience*, 3(9), 608.